Research Square

Preprints are preliminary reports that have not undergone peer review.
They should not be considered conclusive, used to inform clinical practice,
or referenced by the media as validated information.

Three-Dimensional Structure and Spatiotemporal Evolution of Ionospheric Disturbances During the 19--22 January 2026 Geomagnetic Storm

Wenbin Liang
Guilin University of Electronic Technology
Xiyan Sun
sunxiyan1@163.com
Guilin University of Electronic Technology
Yuanfa Ji
Guilin University of Electronic Technology
Xiaodong Ren
Wuhan University
Jianbo Ji
Guilin University of Aerospace Technology
Dengkui Mei
Wuhan University
Xizi Jia
Guilin University of Electronic Technology
Xiuping Li
Guilin University of Electronic Technology
Canhui Jiang
Guilin University of Electronic Technology

Research Article

Keywords:

Posted Date: November 25th, 2026

DOI: https://doi.org/10.21203/rs.3.rs-11610579/v1

License: This work is licensed under a Creative Commons Attribution 4.0 International License.
Read Full License

Additional Declarations: No competing interests reported.

Three-Dimensional Structure and Spatiotemporal Evolution of Ionospheric Disturbances During the 19–22 January 2026 Geomagnetic Storm

Wenbin Liang[1,2], Xiyan Sun[1,4*], Yuanfa Ji[1,4*], Xiaodong Ren[3], Jianbo Ji[2], Dengkui Mei[5], Xizi Jia[1,4], Xiuping Li[1,4], Canhui Jiang[1,4]

[1]School of Information and Communication, Guilin University of Electronic Technology, Guilin, 541004, China .
[2]School of Artificial Intelligence, Guilin University of Aerospace Technology, Guilin, 541004, China .
[3]School of Geodesy and Geomatics, Wuhan University, Wuhan, 430079, China .
[4]International Joint Research Laboratory of Spatio-temporal Information and Intelligent Location Services, Guilin University of Electronic Technology, Guilin, 541004, China .
[5]Chinese Antarctic Center of Surveying and Mapping, Wuhan University, Wuhan, 430079, China .

Abstract

Storm-time total electron content integrates disturbances whose signs and amplitudes can vary with altitude, limiting the interpretation of horizontal maps alone. We formulate multi-pattern propagation–evolution tomography for signed three-dimensional electron-density residuals and examine the accompanying North American disturbance figures for 19–22 January 2026. The framework retains slant-observation geometry on a $\mathbf{1^\circ \times 1^\circ \times 50}$ km grid, separates horizontal pattern propagation from finite evolution increments, and corrects quadratic penalties for the number of additive components. A profiled objective and nuisance-projected sensitivities distinguish regularized total-field estimation from conditional component identifiability. The figure-based analysis shows marked regional contrasts through two geomagnetic intensifications and the subsequent recovery. Between 11:50 on 20 January and 20:00 on 21 January, the magnitude of the symmetric ring-current index decreased by approximately 63%, while localized vertical

TEC residuals near $\pm$**0.6**–**0.8** TECU remained visible. Displayed density contrasts at 175–325 km were commonly of order **2**–**6** $\times$ $\mathbf{10^9}$ electrons m^{-3}. On 21 January, orthogonal sections at **100**°W and **45**°N show horizontal residual contrasts approaching $\pm\mathbf{0.07}\times\mathbf{10^{11}}$ electrons m^{-3}. At **80**°W, **45**°N, the altitude–time field exhibits a positive–negative–positive sequence between 19:00 and 22:00 UTC, with selected profile extrema of approximately $+\mathbf{0.06}$, $-\mathbf{0.065}$, and $+\mathbf{0.045}\times\mathbf{10^{11}}$ electrons m^{-3}. These observations document altitude-dependent residual structure during geomagnetic recovery.

Keywords: ionospheric tomography, global navigation satellite systems, geomagnetic storms, electron-density disturbances, inverse problems

1 Introduction

Geomagnetic storms alter the ionosphere through electric fields, thermospheric circulation, composition changes, and enhanced high-latitude energy deposition. The resulting electron-density field combines redistribution of the background plasma with disturbances propagating through an evolving medium Hunsucker (1982); Buonsanto (1999). Atmospheric gravity waves provide an established explanation for many traveling ionospheric disturbances, but a moving total-electron-content (TEC) pattern does not uniquely identify its driver Hines (1960); Hocke and Schlegel (1996). Plasma instabilities, neutral-wave forcing, and the evolution of large-scale density gradients can produce overlapping signatures Makela and Otsuka (2012); Zhang et al. (2022). Interpreting these signatures requires information about their altitude distribution and temporal evolution, as well as their horizontal displacement.

Altitude dependence matters because background winds select which gravity-wave components penetrate the thermosphere, while dissipation changes their amplitudes and phase relationships Fritts and Vadas (2008); Vadas and Nicolls (2012). Ground-based and low-Earth-orbiting observations have consequently been combined to investigate horizontal and vertical disturbance propagation Ren et al. (2022). Three-dimensional imaging can connect these complementary measurements, provided that resolved structure is distinguished from structure supplied by the representation or regularization Aa et al. (2023). During a storm, positive and negative density perturbations at different heights can partly cancel in an integral measurement. A small integrated residual therefore need not imply a weak perturbation at every altitude.

Global Navigation Satellite System (GNSS) networks offer extensive spatial and temporal sampling. Regional mapping and automated global processing established their value for monitoring TEC variability Saito et al. (1998); Mannucci et al. (1998); Rideout and Coster (2006); subsequent studies characterized both large-scale storm-time disturbances and medium-scale propagation Ding et al. (2007); Hernández-Pajares et al. (2006). Each slant observation nevertheless integrates electron density along a receiver–satellite ray. Mapping it to a nominal ionospheric shell supports horizontal visualization but does not recover the contributing altitude distribution. The background convention also matters: time-variable receiver biases and temporal

detrending can change the amplitude and period content assigned to a disturbance Coster et al. (2013); Guerra et al. (2024). A quantitative reconstruction must therefore define the observed quantity, its preprocessing, and its geometrical relationship to the estimated state.

Computerized ionospheric tomography addresses this geometrical inverse problem. Its early development established the feasibility of density imaging and the limitations imposed by incomplete angular coverage Austen et al. (1988); Raymund et al. (1990); Yeh and Raymund (1991). Subsequent methods introduced alternative parameterizations, regularization, multisensor observations, and time dependence Bust and Mitchell (2008). Additional voxels do not, by themselves, add independent information. Complementary radio-occultation and space-borne GNSS geometries can improve vertical constraints, whereas a ground-based reconstruction remains sensitive to ray coverage and prior structure Angling (2008); Mei et al. (2023b); Muella et al. (2011). Grid spacing must consequently be reported separately from achieved resolution.

Time-dependent tomography and assimilation provide established means of linking observations across epochs Howe et al. (1998); Mitchell and Spencer (2003). IDA3D and GAIM combine measurements with background information or dynamical predictions, with independent measurements playing a central role in validation Bust et al. (2004); Schunk et al. (2004); Scherliess et al. (2006). Motion-aware imaging also predates this study: Spencer and Mitchell incorporated a model-derived drift into reconstructions of rapidly moving polar-cap structures Spencer and Mitchell (2007). The issue considered here is more specific. A signed residual field inferred from detrended slant TEC may contain overlapping patterns that move differently and change amplitude. A temporal constraint evaluated at fixed positions penalizes coherent motion, while a single prescribed transport cannot represent every superposed feature.

Sparse representations offer a complementary constraint. Wavelet methods describe structure at multiple spatial scales Mallat (1989), while compressed-sensing theory identifies recovery conditions for suitable signals and measurement operators Candès et al. (2006); Donoho (2006). Those conditions are not automatically satisfied by regional GNSS ray matrices. Sparse wavelets, empirical-profile dictionaries, and learned dictionaries nevertheless provide useful regularization for ionospheric tomography Panicciari et al. (2015); Zhao et al. (2023); Mei et al. (2023a). Here, all 18 vertical modes of an International Reference Ionosphere profile library are retained Bilitza et al. (2022). This avoids vertical rank truncation; the associated sparsity penalty still supplies an informative prior, and the empirical profiles are not treated as the true storm-time background.

Recent studies have extended tomography to signed disturbance fields. Kong et al. imaged high-latitude and Arctic disturbances during the March 2015 storm Kong et al. (2019). Liang et al. examined three-dimensional pre-storm structure in May 2024 and altitude-dependent eclipse perturbations in April 2024 Liang et al. (2026,?). These studies motivate the present emphasis on how reconstructed structure evolves and when overlapping contributions can be distinguished. Physics-informed approaches provide another route: PINN-SAMI3 incorporates plasma-model equations, whereas TEC2Ne combines TEC-related features, empirical profiles, and additional predictors

to recover station-level profiles Ma et al. (2024); Li et al. (2026). Their states and constraints differ from the direct slant-observation inversion developed here.

Joint motion-reconstruction and metamorphosis formulations show how geometrical change and intensity evolution can be estimated together Burger et al. (2018); Gris et al. (2020); multiple-transport decompositions provide related representations for superposed patterns Reiss et al. (2018); Krah et al. (2025). Applying these ideas to GNSS observations introduces two challenges. First, adding components must not reduce the objective merely by dividing one field among identical copies. Second, a unique regularized density solution need not imply identifiable velocities or a unique decomposition. Evolution increments can compensate for changed propagation, and component fields can exchange equal and opposite structure while preserving their observed sum. This distinction between numerical estimation and identifiability is fundamental Raue et al. (2009). Variable projection supplies a principled way to evaluate propagation after reoptimizing the competing state variables Golub and Pereyra (1973); van Leeuwen and Aravkin (2021).

The 19–22 January 2026 storm is a relevant setting. Published American-sector observations describe concurrent traveling disturbances and large changes in plasma distribution Guan et al. (2026). Equatorial observations show pronounced longitudinal differences, including post-sunset merging of the ionization-anomaly crests over approximately 35° of longitude Karan et al. (2026). These findings establish a heterogeneous event context; they do not prescribe North American disturbance speeds, altitude profiles, or component identities. The present analysis focuses on the North American residual-density field through two geomagnetic intensifications and the subsequent recovery.

We formulate multi-pattern propagation–evolution tomography (MP-PET) for one or two additive signed fields on a fixed three-dimensional grid. The contribution combines component-number-corrected quadratic penalties, a profiled propagation objective with a reduced-gradient expression, and conditional sensitivity diagnostics that admit competing evolution and boundary explanations. The total field is the primary output. Pattern velocity is not identified with plasma drift, and finite evolution increments are not assigned to individual production or loss processes. Alongside this formulation, the available event figures are analyzed quantitatively to determine which horizontal contrasts and altitude-dependent amplitude changes they support. The accompanying evaluation protocol specifies spatially withheld observations, independent synthetic fields, and compatible external profiles Roberts et al. (2017); their performance outcomes are not inferred from the displayed morphology. This separation defines the present contribution and the evidence still required for empirical validation.

2 Data and Methods

2.1 Observations and the disturbance definition

The case study concerns the North American ionosphere during 19–22 January 2026. We define multi-pattern propagation–evolution tomography (MP-PET) for phase-continuous, dual-frequency slant total electron content (sTEC), retaining the line-of-sight geometry throughout the inversion. The primary output is the summed, signed

electron-density residual. Component fields, propagation parameters, and evolution increments are conditional descriptions of that field. The formulation and evaluation design below specify the proposed estimator; the supplied event figures do not establish that the complete protocol, including independent validation, has been executed.

For carrier-phase ranges L_1, L_2 in metres at frequencies $f_1 > f_2$, the geometry-free observable is

$$s_j^{\phi} = \frac{L_{1,j} - L_{2,j}}{40.3 \times 10^{16}(f_2^{-2} - f_1^{-2})} = s_j + c_a + \eta_j, \tag{1}$$

where s_j is physical sTEC in TECU, c_a is a constant ambiguity and instrumental offset on arc a, and η_j contains measurement error and time-variable contributions. One TECU equals 10^{16} electrons m^{-2}. Signal frequencies follow the recorded identifiers; GPS L1/L2 frequencies are 1575.42/1227.60 MHz. A flagged discontinuity, signal change, or receiver reset starts a new arc. A constant offset cancels under detrending, whereas a varying receiver bias can remain Rideout and Coster (2006); Coster et al. (2013).

For the 30-s input interval, the reference residual is

$$y_j = s_j^{\phi} - \frac{1}{121} \sum_{p=-60}^{60} s_{j+p}^{\phi}. \tag{2}$$

The centered window spans 60 min and contains both endpoints. All 121 samples must be valid and belong to one continuous arc. Missing samples are neither interpolated nor bridged; even a short gap invalidates each window that includes it. Accepted arcs span at least 120 min, gaps exceeding 90 s start new arcs, and the retained central observation must have elevation at least 35°. Otherwise valid lower-elevation samples may contribute to its background. No residual-amplitude cutoff is imposed. The background is subtracted once, before selecting at most one sample per arc within 15 s of each 300-s reconstruction epoch.

A moving-mean residual is not an amplitude-preserving physical background separation Guerra et al. (2024). For an uninterrupted sinusoid, the response of (2) is $1 - \sin(121\omega\delta\tau/2)/[121\sin(\omega\delta\tau/2)]$, with $\delta\tau = 30$ s and zero response at zero frequency. Its gains are approximately 0.873 and 1.161 at periods of 25 and 50 min, respectively. These are analytical filter properties, not event measurements. Moreover, filtering along a moving ray does not generally commute with spatial integration. Accordingly, the state below is an observation-compatible residual density, rather than the complete absolute storm-time density departure. The supplement gives the exact preprocessing-discrepancy and covariance decomposition.

The computational domain is 140°–50° W, 10°–65° N, and 100–1000 km in WGS84 ellipsoidal height. A $1° \times 1° \times 50$-km discretization gives $N = 90 \times 55 \times 18 = 89\,100$ constant-density voxels. Straight receiver–satellite rays are intersected with the geodetic voxel boundaries in Earth-centered Cartesian coordinates. Rays leaving the lateral domain within the modeled shell are excluded. With segment length $\ell_{ij,t}$ in metres,

$$\begin{aligned} \mathbf{y}_t &= \mathbf{H}_t\mathbf{u}_t + \boldsymbol{\epsilon}_t, \\ [\mathbf{A}_t]_{ij} &= 10^{-16}\ell_{ij,t}, \quad \mathbf{H}_t = n_0\mathbf{A}_t, \quad \mathbf{x}_t = n_0\mathbf{u}_t, \end{aligned} \tag{3}$$

where $n_0 = 10^{11}$ electrons m^{-3} is fixed for every epoch. Signed states are permitted, with no epoch-wise amplitude normalization. Contributions outside the modeled shell, background incompatibility, discretization, and temporal matching enter $\boldsymbol{\epsilon}_t$. The inversion introduces neither thin-shell vertical mapping nor five-minute averaging. Grid spacing does not establish achieved resolution.

The working error scale uses second differences of $z_j = y_j \sin e_j$, where e_j is elevation:

$$\begin{aligned} \sigma_a &= \max\left\{0.03, \frac{1.4826}{\sqrt{6}}\,\mathrm{MAD}(z_{j+1} - 2z_j + z_{j-1})\right\}, \\ \sigma_i &= \sigma_{a(i)} / \sin e_i. \end{aligned} \tag{4}$$

The scales are in TECU; arcs require at least 40 uninterrupted difference triplets. The factor $\sqrt{6}$ assumes independent equal-variance raw errors and therefore supplies a working scale, not an exact covariance model. We use standardized observations $\widetilde{\mathbf{y}}_t$ and ray matrices $\widetilde{\mathbf{H}}_t$, and Huber loss $\rho_c(r) = r^2/2$ for $|r| \le c$ and $c|r| - c^2/2$ otherwise, with $c = 1.345$ Huber (1964). The 0.03-TECU floor is a declared numerical choice. Overlapping filter windows induce correlated errors that diagonal weighting does not remove.

2.2 Spatial representation and propagation–evolution model

An offline IRI-2020 library defines a complete vertical coordinate system Bilitza et al. (2022). The reference sampling comprises 98 496 normalized profiles: 19 longitude nodes, 12 latitude nodes, 36 monthly dates in 2020, 2022, and 2023, and 12 two-hourly epochs per date. An SVD supplies an orthonormal 18×18 matrix $\mathbf{D}_h$; all 18 vectors are retained. Thus no vertical rank truncation is imposed, although sparsity in this basis remains an informative prior. Event observations and validation profiles do not enter its construction. The specified IRI options, input-index records, basis matrix, and singular values must accompany an executable run.

Let $\mathbf{P}$ arrange horizontal maps, $\mathbf{E}$ mirror-extend each 90×55 map to 96×56 without repeated endpoints, and $\mathbf{Q}_H$ apply three orthonormal Haar levels. The analysis operators are

$$\begin{aligned} \mathbf{S} &= \mathbf{Q}_H \mathbf{E} \mathbf{P} (\mathbf{I}_{4950} \otimes \mathbf{D}_h^{\mathsf{T}}), \\ \mathbf{S}_q &= \mathbf{Q}_H \mathbf{E} \mathbf{P}. \end{aligned} \tag{5}$$

Both produce 96 768 coefficients per epoch. Unlike $\mathbf{S}$, the increment operator $\mathbf{S}_q$ acts independently on physical height layers. The adjoint of the non-square extension accumulates repeated boundary samples; cropping is not its transpose. Approximation and detail coefficients are both penalized.

For $K \in \{1, 2\}$, the observation-compatible field is a sum of simultaneously estimated patterns,

$$\mathbf{u}_t = \sum_{k=1}^{K} \mathbf{u}_t^{(k)}. \tag{6}$$

Components may overlap and interfere; they are not assigned prescribed physical drivers. Their horizontal pattern velocities use cubic B-splines at 5° horizontal knot spacing, linear interpolation at heights 150, 275, 450, and 775 km, and 30-min temporal control spacing. Multiplying the dimensionless controls by $v_0 = 1000\ \mathrm{m\,s}^{-1}$ gives

physical velocities. Each two-component control vector is bounded by 1.5; nonnegative partition-of-unity interpolation therefore bounds speed by 1500 $\mathrm{m\,s^{-1}}$. This is a search constraint, not an assumed event speed. A 120-min window has 11 760 scalar velocity controls per pattern.

A same-height warp $\mathbf{W}_t^{(k)}$ backtracks characteristics through WGS84 eastward and northward metric factors using five explicit-midpoint steps of -60 s. Values are interpolated with the 4×4 Keys cubic-convolution stencil Keys (1981). The operation approximates center values and is not a conservative finite-volume remap. It changes neither altitude nor interlayer phase alignment. Its transpose scatters the same interpolation weights. A fixed interior selector $\mathbf{M}$ excludes boundary locations whose full admissible characteristic stencil cannot be evaluated. Propagation consistency is

$$\mathbf{r}_t^{(k)} = \mathbf{M}\left[\mathbf{u}_{t+1}^{(k)} - \mathbf{W}_t^{(k)}\mathbf{u}_t^{(k)} - \mathbf{q}_t^{(k)}\right]. \tag{7}$$

The dimensionless increment $\mathbf{q}_t^{(k)}$ describes the finite 300-s change unexplained by horizontal propagation; its physical scale is $n_0\mathbf{q}_t^{(k)}$. It is estimated jointly with the states, rather than equated to the entire propagation residual. Three directional Haar details at a common location, scale, height, and interval form an increment group; coarsest coefficients form singleton groups. Groups do not couple different heights or times.

Pattern velocities need not equal plasma drift. Production, loss, compressibility, vertical transport, evolving background conditions, and the difference between pattern and plasma velocities can all enter the effective increment. The supplement derives this distinction from electron continuity. Consequently, neither a fitted increment nor a signed component is interpreted as a separately conserved plasma population or an independently measured production rate.

2.3 Objective and mathematical properties

Stack states and increments in $\mathbf{z} \in \mathbb{R}^{KN(2T-1)}$ and velocity controls in $\mathbf{\Theta} \in \mathcal{C}_K$. Define $N_y = \sum_t m_t$, $D_d = (T-1)N_M$, $N_q = (T-1)P_q$, and $D_z = N(2T-1)$, where N_M is the interior-mask size and $P_s = P_q = 96\,768$. The normalized penalties are

$$\begin{aligned}
J_y &= N_y^{-1} \sum_{t,i} \rho_c\Big([\widetilde{\mathbf{H}}_t \textstyle\sum_k \mathbf{u}_t^{(k)} - \widetilde{\mathbf{y}}_t]_i\Big), \\
J_s &= (TP_s)^{-1} \sum_{k,t} \|\mathbf{S}\mathbf{u}_t^{(k)}\|_1, \\
J_d &= (2D_d)^{-1} \sum_{k,t} \|\mathbf{r}_t^{(k)}\|_2^2, \\
J_q &= N_q^{-1} \sum_{k,t,g} \sqrt{|g|}\,\|[\mathbf{S}_q\mathbf{q}_t^{(k)}]_g\|_2.
\end{aligned} \tag{8}$$

Table 1 Declared reference configuration of MP-PET. These settings specify the estimator; they are not experimentally established optima or measured event properties.

Quantity	Reference setting
Domain / grid	140–50° W, 10–65° N, 100–1000 km; $1^\circ \times 1^\circ \times 50$ km
Input / state interval	30 s / 300 s
Background / arc length	60-min centered mean / ≥ 120 min
Elevation / epoch match	35° / ± 15 s
Window / advance	120 min (25 epochs) / 60 min
Retained interval	$[30, 90)$ min within each window
Density / speed scale	10^{11} electrons m^{-3} / 1000 $\mathrm{m\,s}^{-1}$
Component count / starts	$K = 1, 2$ / ten per count
$(\lambda_s, \beta, \lambda_q)$	$(0.01, 5, 0.20)$
$(\lambda_{vh}, \lambda_{vt}, \lambda_{vz})$	$(0.05, 0.05, 0.01)$
$(\lambda_{v0}, \varepsilon)$	$(10^{-4}, 10^{-6})$
Independent spatial test	20% of occupied 2° blocks
Development selection	Five folds; nine configurations

MP-PET minimizes

$$\mathcal{J}_K = J_y + \lambda_s J_s + K\beta J_d + \lambda_q J_q + \sum_k \mathcal{R}_v(\boldsymbol{\theta}^{(k)}) + \frac{K\varepsilon}{2D_z}\|\mathbf{z}\|_2^2. \tag{9}$$

The velocity prior $\mathcal{R}_v$ penalizes adjacent-control differences in horizontal position, time, and height, normalized by 500 km, 1800 s, and 100 km, respectively, and includes a small control ridge. It regularizes motion without averaging density states between layers. All reference weights are dimensionless (Table 1).

Proposition 1 (duplication control). If all K components share controls $\boldsymbol{\theta}$, their summed states and increments satisfy

$$\mathcal{J}_K \geq \mathcal{J}_1 + (K-1)\mathcal{R}_v(\boldsymbol{\theta}). \tag{10}$$

The data terms agree; linearity, triangle inequalities, and $\|\sum_k \mathbf{a}_k\|^2 \leq K\sum_k \|\mathbf{a}_k\|^2$ establish the result. Thus dividing one pattern into equal copies cannot lower its state-dependent penalties. This removes a specific model-count artifact, but does not establish component identifiability. Appending a zero component is not penalty-preserving, so regularized objective differences are not likelihood-ratio statistics.

Proposition 2 (conditional well-posedness). At fixed controls, (9) is strongly convex in $\mathbf{z}$, with modulus $\mu_K = K\varepsilon/D_z > 0$, and has a unique minimizer. Continuity, uniform coercivity, and compact control bounds imply existence of a joint global minimizer. The joint problem remains nonconvex; numerical optimization need not find that minimizer. Uniqueness of the regularized conditional state is not uniqueness of its physical explanation.

2.4 Profiled solution and conditional identifiability

We minimize the profiled objective

$$\Phi_K(\boldsymbol{\Theta}) = \mathcal{J}_K(\mathbf{z}_*(\boldsymbol{\Theta}), \boldsymbol{\Theta}), \quad \mathbf{z}_* = \arg\min_{\mathbf{z}} \mathcal{J}_K. \tag{11}$$

States and increments are reoptimized at every trial control field. This distinguishes variable projection from a velocity update evaluated against a frozen reconstruction Golub and Pereyra (1973); van Leeuwen and Aravkin (2021). Let $a_d = K\beta/D_d$ and $\mathbf{G}_t^{(k)}\mathbf{d} = \mathbf{M}\{[\partial_\theta \mathbf{W}_t^{(k)}\mathbf{d}]\mathbf{u}_t^{(k)}\}$.

Proposition 3 (reduced gradient). Where the discretized warp has a continuous control derivative, the unique inner minimizer and minimum-value envelope theorem give

$$\nabla_{\theta^{(k)}} \Phi_K = -a_d \sum_t [\mathbf{G}_t^{(k)}]^\mathsf{T} \mathbf{r}_t^{(k)} + \nabla \mathcal{R}_v. \tag{12}$$

No additional chain-rule term is needed at the accurately solved inner optimum. On a stable active face, away from Huber transitions and interpolation second-derivative breakpoints, the reduced Hessian is the Schur complement $\mathbf{H}_{\Theta\Theta} - \mathbf{H}_{\Theta\xi}\mathbf{H}_{\xi\xi}^{-1}\mathbf{H}_{\xi\Theta}$. It measures regularized curvature, not data-only information; the unrestricted classical Hessian is not used at active-set changes or active speed bounds.

The fixed-control problem is solved by a primal–dual splitting with exact proximal maps for Huber fidelity, spatial sparsity, grouped increments, and the ridge Chambolle and Pock (2011). The supplement provides the scaling, adjoints, certified step bound, and primal/dual objectives P, D, for which $D \le \Phi_K \le P$. Projected-gradient trials resolve the inner problem. A bound-based acceptance test certifies profile decrease when the trial upper bound lies below the current lower bound plus the negative Armijo term. A separate refinement-based test can establish numerically resolved computed descent, but is explicitly noncertifying. The small ridge matters: for $T = 25$, $D_z = 4\,365\,900$ and $K = 2$ gives $\mu_K \simeq 4.58 \times 10^{-13}$. A small objective gap consequently need not bound component errors tightly.

Propagation itself is structurally ambiguous if increments are unrestricted. Changing θ to θ' can be absorbed exactly by

$$\mathbf{q}_t'^{(k)} = \mathbf{q}_t^{(k)} + [\mathbf{W}_t^{(k)}(\theta) - \mathbf{W}_t^{(k)}(\theta')]\mathbf{u}_t^{(k)}, \tag{13}$$

leaving observations and propagation residuals unchanged. Equal-and-opposite component exchange also preserves the summed field. We therefore assess local sensitivity conditional on an explicit admissible nuisance family. Let $\mathbf{B}_\Theta$ and $\mathbf{B}_\xi$ be observation Jacobians for controls and allowed initial-state, increment, boundary, and mismatch changes. Then

$$\mathbf{I}_{\mathrm{cond}} = \mathbf{B}_\Theta^\mathsf{T}(\mathbf{I} - \mathbf{B}_\xi \mathbf{B}_\xi^\dagger)\mathbf{B}_\Theta. \tag{14}$$

Proposition 4 (nuisance expansion). Enlarging the nuisance range cannot increase any directional value of (14); unrestricted increments or evolution mismatches give zero sensitivity by (13). This follows directly by minimizing the squared observation change over an enlarged nuisance space.

The protocol compares fitted stable supports, a prescribed neighbouring-support expansion, and unrestricted limits, retaining boundary freedoms. It tests 40 named directions per component: eastward and northward perturbations of 100 $\mathrm{m\,s^{-1}}$ at each of four height and five time controls. These directions sample a declared subset of the control space. Numerical rank, support-dependent sensitivity, and empirical noise-limited recovery are distinct. For an ideal fully observed Fourier mode, the two-column

temporal Gram matrix has eigenvalues $T \pm |\sin(T\Delta\Omega/2)/\sin(\Delta\Omega/2)|$. Nonaliased, *prescribed* component frequencies make their complex amplitudes identifiable for $T \geq 2$; this does not identify two unknown frequencies or full velocity vectors from two epochs. Near coincidence, the smaller eigenvalue decreases quadratically. The supplement develops this separation limit and the separate aperture ambiguity.

2.5 Evaluation design and numerical reporting

The evaluation protocol uses fixed $2^\circ \times 2^\circ$ station blocks, anchored at 140° W and 10° N, with seed 20261011. Twenty percent of occupied blocks are withheld from all fitting and selection; the remainder form five development folds. At least 25 occupied blocks are required. Block-balanced squared prediction errors compare nine configurations for each K: the reference settings and separate half/double changes in spatial, propagation, and increment weights, plus joint half/double velocity-smoothness changes. A one-standard-error rule favors the smallest admissible K Roberts et al. (2017). Frozen settings then define a refit on non-test stations. No independent-test result, visual rendering, or expected published velocity enters selection.

Required predictive outputs are held-out sTEC RMSE, absolute error, signed bias, and 5–30-min residual autocorrelation. They test path-integrated predictions rather than altitude allocation. Independent density profiles require compatible backgrounds and vertical support, matching within 5 min and 100 km, and averaging to the same 50-km layers. Missing profile sequences cannot be interpolated merely to construct a compatible background. Without such observations, altitude validation remains unavailable.

The prescribed synthetic suite uses a finer $0.25^\circ \times 0.25^\circ \times 10$-km grid at 30 s, independently of the inversion dictionary. Reference 600-km/400-m s^{-1} and 1800-km/600-m s^{-1} packets have periods of 25 and 50 min; tests include growth, decay, interlayer phase, counter-propagation, standing interference, nearly coincident branches, and noise. Thirty realizations per primary scenario use 0.05-TECU noise, with additional noise, station-loss, gap, correlation, and outlier sensitivities. Two hundred noise-only runs define an empirical amplitude threshold. Algorithm-isolation tests integrate signed truth directly; end-to-end controls inject bounded perturbations into an absolute background and repeat the complete preprocessing chain. A 120-min valid interval requires 180 min of raw data for the centered 60-min filter, or 150/210 min for the 30/90-min sensitivity filters. The 8-min control tests aliasing; primary interpretation is restricted to periods of at least 20 min.

For a synthetic field averaged over reconstruction voxels, the total-field error is

$$E_{\mathrm{tot}} = \left[\frac{\sum_{j,t} V_j (\widehat{x}_{j,t} - x^*_{j,t})^2}{\sum_{j,t} V_j (x^*_{j,t})^2} \right]^{1/2}, \tag{15}$$

where V_j is voxel volume. Component errors use the analogous sum over components and the best single label permutation for the complete window; zero-disturbance tests instead use absolute error and reconstructed energy. Fitting sine and cosine coefficients at a prescribed synthetic frequency provides amplitude and phase, with phase

interpreted only above the noise-calibrated amplitude threshold. These distinctions prevent a satisfactory summed prediction from concealing an unstable decomposition. A plane wave constrains only velocity along its wavevector, so its reported velocity error concerns that normal component. The synthetic reference amplitude is 5×10^{10} electrons m^{-3}, with a 325-km central height and a 100-km vertical envelope width. These prescribed values test the estimator and are not assigned to the January event.

Baselines separate propagation, increments, temporal coupling, additional model capacity, and post-reconstruction decomposition. Volume-weighted errors distinguish total-field from label-matched component recovery without phase shifting or amplitude rescaling. The design specifies 2000 paired spatial/time-block bootstrap replicates for summary metrics, with 60-min blocks within fixed 6-h strata Künsch (1989). These are evaluation requirements, not accuracy, uncertainty, or significance results available for the present figures.

Initialization uses a training-only independent-epoch sparse reconstruction and a bounded linearized advection fit. For one component, the ten seeds are zero, the linearized field, and uniform velocities of $\pm 400\ \mathrm{m\,s^{-1}}$ along four axes separated by 45°. For two components, duplicated initial seeds, counter-propagating pairs, and pairs offset by $\pm 300\ \mathrm{m\,s^{-1}}$ from the linearized field provide ten comparable starts. They explore the nonconvex objective without prescribing a recovered direction. Candidate comparison retains the lowest sufficiently resolved training objective within a fixed count and configuration; failed fits remain failures rather than being removed from difficult folds.

The inner criterion requires normalized primal and dual fixed-point residuals no greater than 10^{-5} and relative state change below 10^{-6} at two successive checks, 50 iterations apart. Refinement tightens these thresholds tenfold. Practical outer stability requires objective change below 10^{-4}, total-field change below 10^{-3}, and velocity RMS change below $10\ \mathrm{m\,s^{-1}}$ for three accepted updates. These are numerical stopping rules. The separate first-order certificate requires a bounded gradient error and a projected-gradient residual no greater than 10^{-6}. Adjoint identities, ray-length closure within 1 m, differentiated-warp checks, and equal-velocity duplication checks are required before interpreting an implementation. Matrix-free wavelets and warps avoid a dense space–time matrix, but repeated profiled inner solves can be expensive; equal iteration budgets do not demonstrate equal runtime.

Each 120-min inversion window contains 25 epochs, advances by 60 min, and contributes only its central $[30, 90)$ min. Adjacent estimates are not amplitude-matched or smoothed; the method is an offline smoother. Both model counts use ten deterministic starts, at most 30 accepted outer updates, and 5000 inner iterations, extendable to 20 000 during refinement. Separate flags record coverage, numerical stability, certified decrease, stationarity, and conditional sensitivity. A total field may remain reportable with `DECOMPOSITION_UNRESOLVED`. This flag does not imply that only one physical wave existed. Operator checks and numerical convergence establish implementation consistency, not scientific accuracy; measured performance and resource use require the execution records specified in the supplement.

3 Results

The analysis below concerns the displayed total perturbation field and its relationship to the TEC diagnostics. Values read from color scales and plotted trajectories are approximate; the stated ranges describe resolved features in the figures rather than confidence intervals or extrema inferred beyond the plotting limits. All times are UTC. Absolute timestamps are used to align the panels with the two storm intensifications, including where the original images retain broader phase labels.

3.1 Storm Development and Observational Support

The mapped GNSS receivers span approximately 125°–67°W and 25°–49°N, with visibly uneven station density across the continental United States [Fig. 1(a)]. The event developed through two pronounced geomagnetic intensifications. The first SYM-H depression reached approximately −240 nT late on 19 January, accompanied by AE exceeding 4000 nT. Available solar-wind observations increased from approximately 450 to 1000–1100 $\mathrm{km\,s^{-1}}$, and dynamic pressure subsequently approached 90 nPa near 00:00 on 20 January [Fig. 1(b)–(f)]. Gaps in the upstream records interrupt the forcing history during the initial decline; the displayed curves therefore do not provide a continuous account of the solar-wind conditions leading to the first minimum.

A second intensification followed partial geomagnetic recovery on 20 January. In the available record, the northward IMF excursion of approximately +50 to +60 nT late on 19 January was followed by southward values of approximately −20 to −30 nT on the following morning. Dynamic pressure again reached approximately 40–50 nPa, AE exceeded 4000 nT, and SYM-H decreased to approximately −250 nT. The sequence agrees with the published chronology: a sudden storm commencement at 19:24 on 19 January, a first minimum of −243 nT at 21:42, and renewed intensification from 09:23 on 20 January, followed by an event minimum of −252 nT Gordiyenko et al. (2026). These timings distinguish the partially recovered 08:00 snapshot from the subsequent second intensification.

During 21–22 January, solar-wind speed decreased toward 500–600 $\mathrm{km\,s^{-1}}$ and SYM-H recovered to approximately −50 to −80 nT. AE was generally lower on 22 January but increased again to approximately 1000 nT near the end of the interval. Thus, the four-day window encompasses two major intensifications and an extended, intermittently disturbed recovery. This distinction is relevant to the spatial comparisons below and is consistent with reports of both main-phase and recovery-phase disturbances over the American sector Guan et al. (2026).

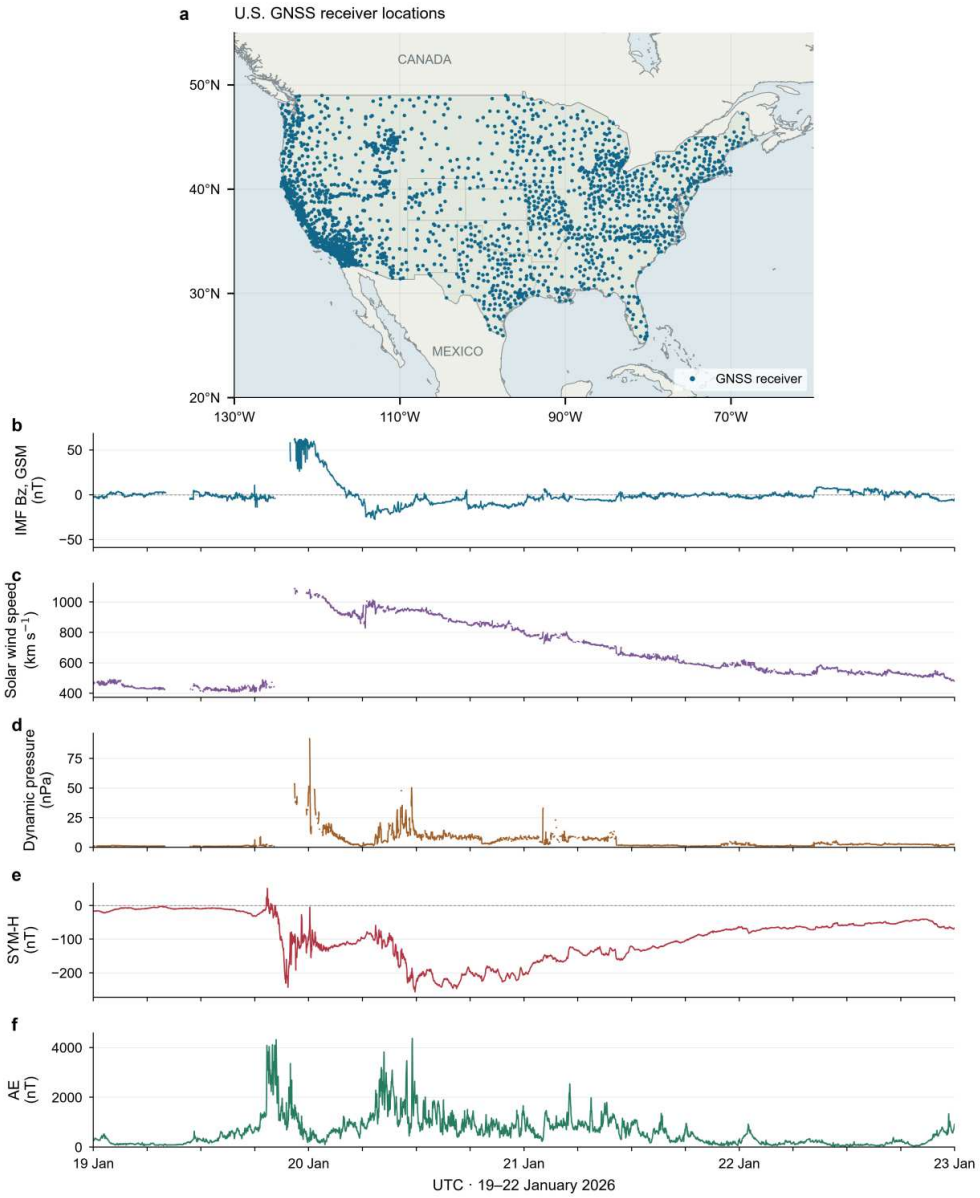


Fig. 1 GNSS receiver distribution and interplanetary and geomagnetic conditions during 19–22 January 2026. (a) Receiver locations over the continental United States. (b) North–south interplanetary magnetic-field component, B_z, in geocentric solar magnetospheric coordinates (nT). (c) Solar-wind speed ($\mathrm{km\,s^{-1}}$). (d) Solar-wind dynamic pressure (nPa). (e) SYM-H and (f) AE indices (nT). Panels (b)–(f) share the UTC axis from 00:00 on 19 January to 00:00 on 23 January. The horizontal dotted line in (e) denotes zero SYM-H; discontinuities mark gaps in the plotted records.

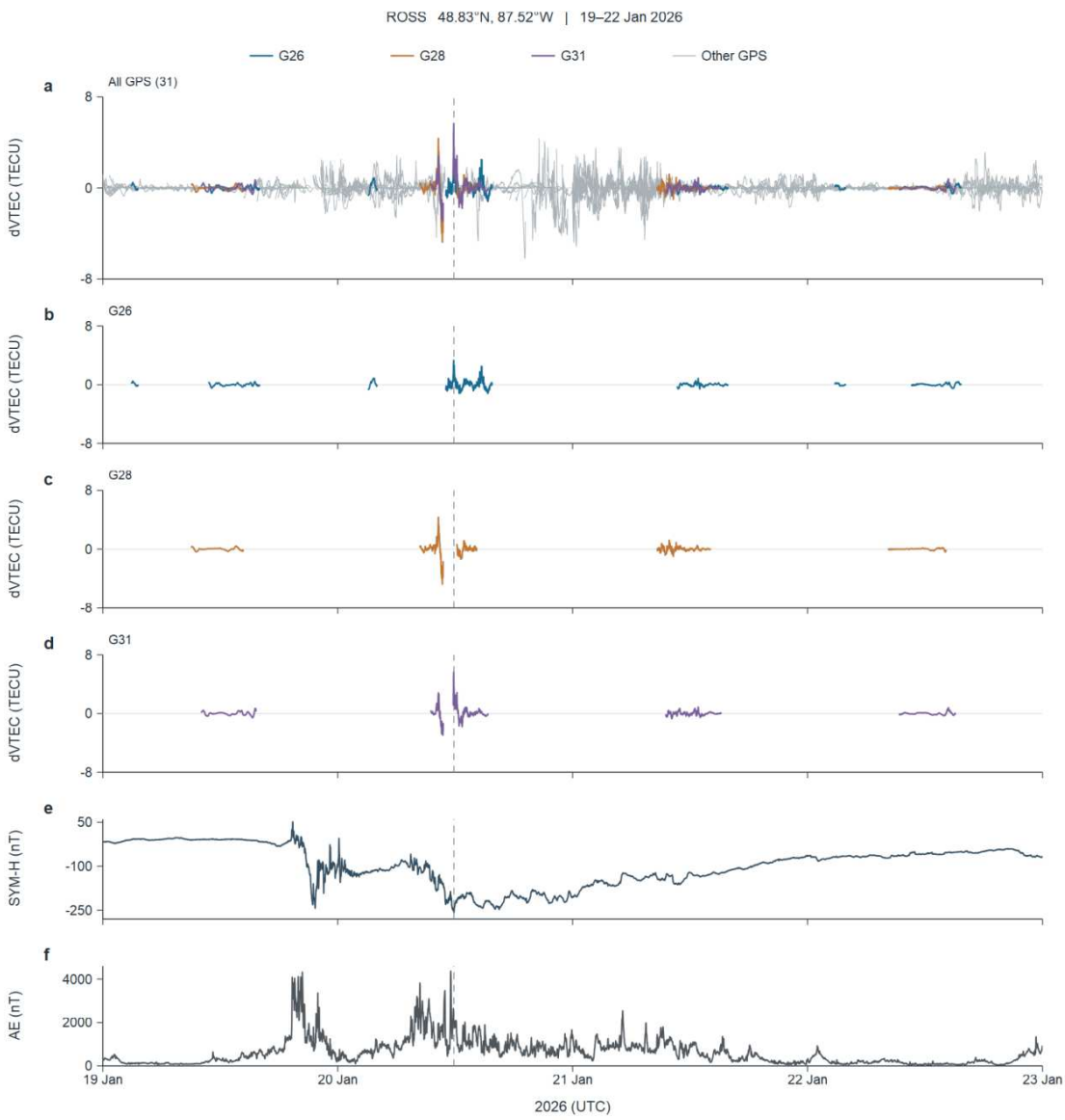


Fig. 2 Multisatellite dVTEC observations at ROSS (48.83°N, 87.52°W) and concurrent geomagnetic activity during 19–22 January 2026. (a) All 31 GPS satellites represented over the interval; G26, G28, and G31 are highlighted in blue, orange, and purple, with other links in gray. (b)–(d) Individual G26, G28, and G31 records on identical dVTEC scales (TECU). (e) SYM-H and (f) AE (nT). The common axis extends from 00:00 on 19 January to 00:00 on 23 January UTC. The dashed line is approximately 12:00 on 20 January. Gaps indicate intervals without plotted values for the corresponding link. Extrema across different links in (a) are not interpreted as a single-arc peak-to-peak amplitude.

3.2 Station-Scale Variability and Spatial Contrasts

Figure 2 combines observations from the 31 GPS satellites represented at ROSS (48.83°N, 87.52°W) over 19–22 January 2026. Within approximately 09:00–15:00 on 20 January, G26 reaches about +3 and −1 to −1.5 TECU, giving a peak-to-peak range of approximately 4–5 TECU. G28 reaches approximately +4 to +4.5 and −4.5 to −5 TECU, giving about 9 TECU. G31 has a positive maximum of approximately +5.5 to +6 TECU and a negative excursion of approximately −2.5 to −3 TECU, giving about 8–9 TECU. The difference between the positive and negative excursions is therefore link dependent even during the same broad interval.

The combined record contains further excursions of approximately −6 and +4 to +4.5 TECU between 18:00 on 20 January and 08:00 on 21 January. These are bounds across different links rather than the two extrema of one traced disturbance. Positive excursions of approximately +3 TECU are also visible late on 22 January. The highlighted G26/G28/G31 arcs do not encompass all subsequent activity at this station, and their weaker available arcs on the surrounding days cannot establish regional disappearance of the disturbance.

The stations in Fig. 3 sample complementary spatial separations. ALDO and NSCI differ by 11.5° in the reported magnetic latitude and only 0.96° in geographic longitude, corresponding to approximately 3.8 min of mean local solar time. NSCI and URI1 differ by 1.0° in magnetic latitude and 12.95° in longitude, corresponding to approximately 51.8 min. These separations facilitate comparison of the sampled responses, but do not remove differences in ray geometry or satellite coverage.

The three columns are treated as Intervals I–III, using their timestamps rather than the original phase headings. Interval I covers approximately 20–21 on 19 January to 00:00 on 20 January. Interval II covers approximately 00:00–12:00 on 20 January and includes partial recovery as well as renewed intensification. Interval III extends approximately from 12:00 on 20 January to 16:00 on 22 January. During Interval I, ALDO observations lie roughly between −0.15 and +0.25 TECU, selected URI1 excursions are of order 0.3 TECU, and some NSCI trajectories reach the ±0.5 TECU display boundaries. Several trajectories at all three stations reach those boundaries in later intervals. The near-zero 3-h medians describe the central tendency of signed residuals and are not amplitude estimates; clipping prevents reliable comparison of the true extrema.

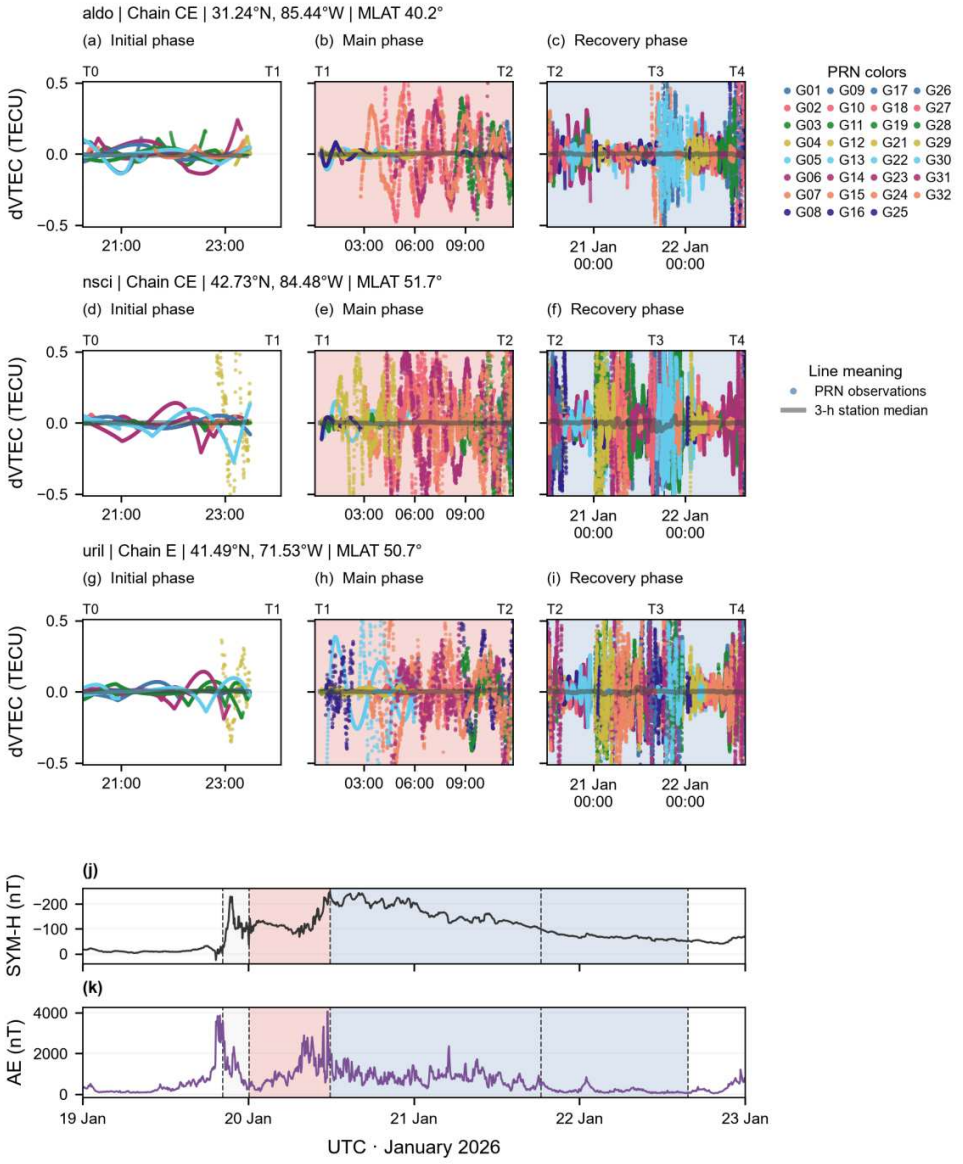


Fig. 3 dVTEC at ALDO (31.24°N, 85.44°W; reported MLAT 40.2°), NSCI (42.73°N, 84.48°W; MLAT 51.7°), and URI1 (41.49°N, 71.53°W; MLAT 50.7°), in panels (a)–(c), (d)–(f), and (g)–(i), respectively. Columns are interpreted as Interval I (approximately 20–21 on 19 January to 00:00 on 20 January), Interval II (00:00–12:00 on 20 January), and Interval III (12:00 on 20 January to 16:00 on 22 January), all in 2026 UTC; their time scales differ. T3 denotes approximately 18:00 on 21 January. Colors identify PRNs, and thick gray curves are 3-h station medians. The ±0.5 TECU range clips some trajectories. Panels (j) and (k) show SYM-H and AE; the SYM-H ordinate is inverted. The original phase headings are retained in the image, but the interval definitions above determine the interpretation.

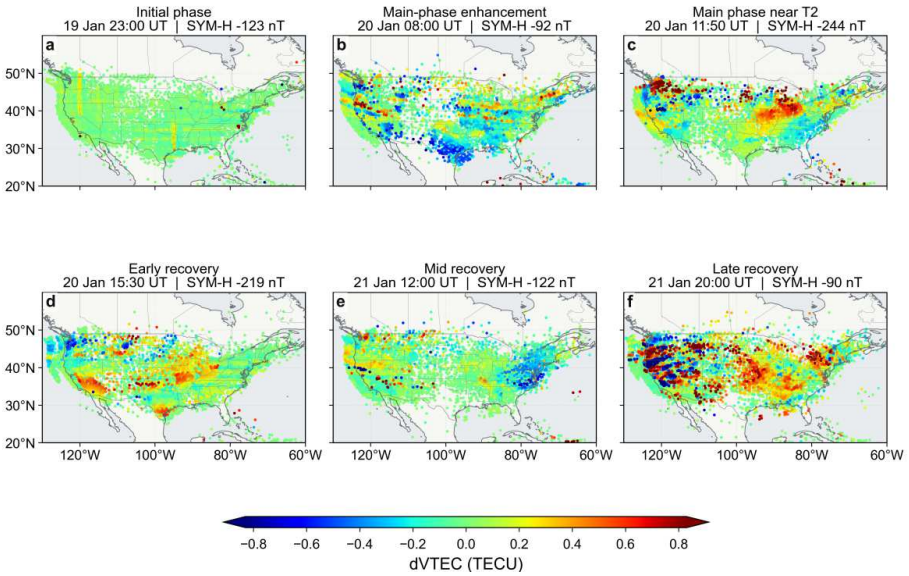


Fig. 4 Regional detrended vertical total electron content (dVTEC) at six selected epochs. Times and SYM-H values are (a) 19 January, 23:00, −123 nT; (b) 20 January, 08:00, −92 nT; (c) 20 January, 11:50, −244 nT; (d) 20 January, 15:30, −219 nT; (e) 21 January, 12:00, −122 nT; and (f) 21 January, 20:00, −90 nT, all in 2026 UTC. Colors show signed dVTEC at plotted locations, with common labeled ticks from −0.8 to +0.8 TECU in 0.2-TECU increments and extensions at both ends. All panels span approximately 130°–60°W and 20°–60°N. Temporal interpretation follows the timestamps: (a) follows the first SYM-H minimum and (b) precedes the second intensification, notwithstanding the original phase headings. Unplotted areas do not imply zero perturbation.

3.3 Horizontal Organization of TEC Disturbances

The six regional dVTEC snapshots span 45 h and show substantial changes in the location and polarity of the strongest displayed perturbations (Fig. 4). At 23:00 on 19 January, most sampled locations lie within approximately −0.2 to +0.2 TECU. By 08:00 on 20 January, negative values of approximately −0.8 to −0.6 TECU occupy parts of the south-central sector, around 105°–95°W and 25°–35°N. Opposite signs occur over the western sector at the same epoch, demonstrating that the regional response cannot be represented by a single signed enhancement or depletion.

Near the second SYM-H minimum, at 11:50 on 20 January, positive clusters of approximately +0.6 to +0.8 TECU appear within 100°–85°W and 35°–45°N. Negative values of approximately −0.8 to −0.4 TECU remain locally within the western region, around 125°–105°W and 40°–50°N. At 15:30, positive values of approximately +0.4 to +0.8 TECU extend across parts of the southwest, around 120°–110°W and 30°–40°N, and the central sector, around 105°–90°W and 35°–45°N. Negative clusters persist along the northern part of the western region. These ranges identify local features within geographically mixed fields; they do not assign a uniform sign to each enclosing region.

Spatial contrast remained evident during recovery. At 12:00 on 21 January, an eastern negative feature occupies approximately 85°–70°W and 35°–45°N, with displayed values of about −0.6 to −0.2 TECU. Eight hours later, interspersed positive and negative features in the west reach displayed intervals of +0.6 to +0.8 and −0.8 to −0.6 TECU. Between 11:50 on 20 January and 20:00 on 21 January, SYM-H increases from −244 to −90 nT over 32 h 10 min, a recovery of 154 nT, or approximately 63% of its earlier absolute magnitude. Substantial regional perturbation structure nevertheless remains in the final snapshot.

Two additional comparisons illustrate the limited correspondence between a global storm index and a regional residual map. The 19 January 23:00 and 21 January 12:00 snapshots differ in SYM-H by only 1 nT (−123 versus −122 nT), yet their eastern perturbation distributions differ markedly. Similarly, the 20 January 08:00 and 21 January 20:00 snapshots differ by only 2 nT (−92 versus −90 nT), while the strongest displayed contrasts shift from the south-central sector to a more extensive western pattern. These comparisons include changes in local time and viewing geometry, so they do not isolate a driver. They establish that storm-index magnitude alone does not describe the observed spatial organization.

The snapshot spacing also constrains the temporal interpretation. The first two maps are separated by 9 h, the three maps on 20 January by 230 and 220 min, and the final two by 8 h. A 20 h 30 min gap separates 15:30 on 20 January from 12:00 on 21 January. The maps therefore compare distinct regional states rather than continuously tracking a single crest across the storm. Their strongest supported temporal conclusion is recurrence and reorganization of substantial residual structure, including during recovery, rather than persistence of an individually identified wave throughout the 45-h sequence.

Movies S4, S6, and S7 provide 15-min regional dVTEC sequences centered at 15:30:12 on 20 January and 12:00:12 and 20:00:12 on 21 January, respectively, with times labeled UT in the source frames (Supplementary Note S6). These sequences complement the corresponding selected maps and show changes within the individual observation windows.

3.4 Coordinate–Time Organization

Figures 5 and 6 share an approximately 08:40–12:40 UT window, but the calendar date is absent from the source figures and captions. Their metadata refers to Sobel or edge-weighted processing without specifying its implementation. Accordingly, the displayed color values are retained as labeled, while the relationship to unmodified dVTEC, the aggregation rule, and the calendar-date assignment remain unverified.

In Fig. 5, four geographic-latitude bands are centered at 45°, 40°, 35°, and 30°N, each with half-width 2.5°; together they cover 27.5°–47.5°N. Prominent negative structures in the three northern panels occur near 75°–80°W at 11:30–12:00 and extend toward 85°–95°W at 12:10–12:40. Dark positive and negative portions approach the displayed intervals +0.15 to +0.20 and −0.20 to −0.15 TECU. At 40°N, a positive feature shifts from around 80°W at 11:00 toward 90°–95°W at 12:00, corresponding to an apparent longitudinal displacement of roughly 10°–15° per hour in this section. This

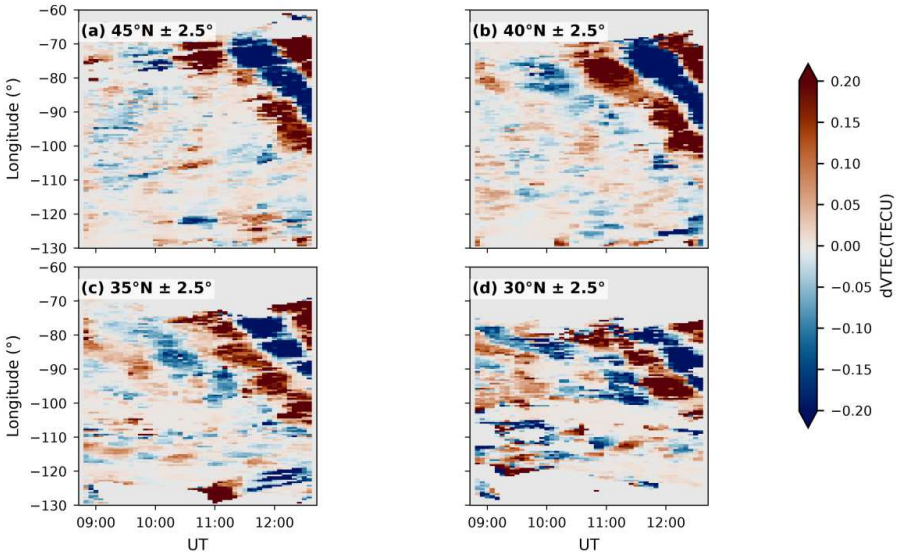


Fig. 5 Longitude–time display within geographic-latitude bands centered at (a) 45°N, (b) 40°N, (c) 35°N, and (d) 30°N, each with a 2.5° half-width. Panels span approximately 08:40–12:40 UT and 60°–130°W, with western longitudes toward the bottom. The source color bar is labeled dVTEC (TECU), with ticks from −0.20 to +0.20 at intervals of 0.05 and extensions at both ends. The source does not specify the calendar date or the Sobel/edge-weighted processing indicated by its metadata. This display is retained as a provisional morphological diagnostic; its slopes are not identified with a three-dimensional propagation velocity.

slope is an intersection trajectory in a finite latitude band, not a measured horizontal velocity vector.

Figure 6 instead samples 100°, 90°, 80°, and 70°W, each with half-width 2.5°, over 20°–60° magnetic latitude. The structures vary among longitude bands. For example, the large negative feature at 80°W reaches higher magnetic latitudes at later times, which is inconsistent with assigning every feature a common equatorward trajectory. The magnetic coordinate system and metric are unspecified, so a conversion using a constant geographic distance per degree is not justified Emmert et al. (2010). Combining a longitudinal slope in one figure with a latitudinal slope in another would additionally require matching the same phase feature, observing geometry, and processing. Satellite motion can affect TEC-based propagation diagnostics Penney and Jackson-Booth (2015); no corrected propagation speed is derived here.

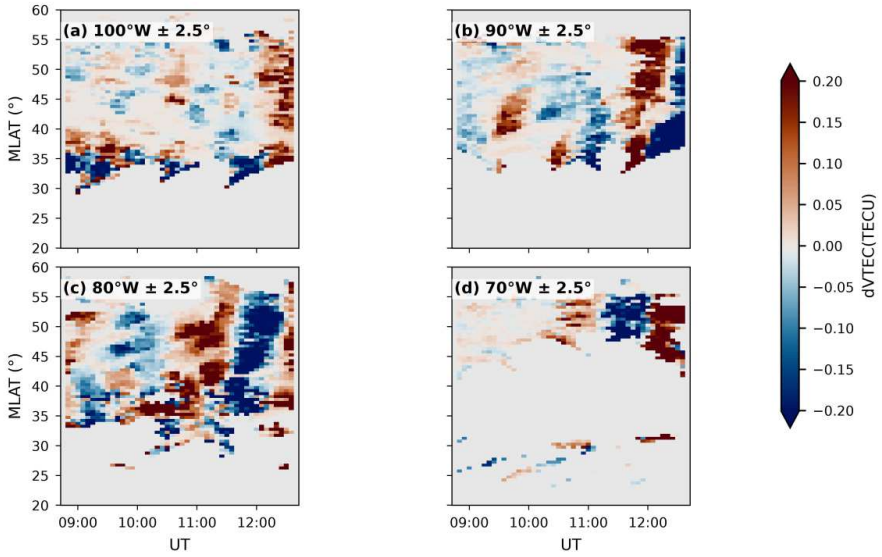


Fig. 6 Magnetic-latitude–time display within longitude bands centered at (a) 100°W, (b) 90°W, (c) 80°W, and (d) 70°W, each with a 2.5° half-width. Panels cover approximately 08:40–12:40 UT and 20°–60° magnetic latitude. The source color bar is labeled dVTEC (TECU), with ticks from −0.20 to +0.20 at intervals of 0.05 and extensions at both ends. Unfilled regions contain no displayed values. The calendar date, magnetic-coordinate definition, aggregation, and Sobel/edge-weighted processing are unspecified, so no physical speed or conversion from magnetic latitude to distance is assigned.

3.5 Radial Structure on 19 January

The radial matrix in Fig. 7 is dated 19 January 2026 and covers 20:00–23:40, or 220 min. Its reference center is 29°N, 97°W; this geometric center is not an identified source. The labeled azimuths are 0°, 30°, 60°, 150°, 120°, and 90°. A clockwise-from-geographic-north convention is used only as the earlier working interpretation, because the source does not document the convention. In the first three panels, early positive values at approximately 1300–2000 km coexist with negative values at approximately 0–700 km. Later, negative outer structure accompanies positive residuals within approximately 0–600 km. The color ticks include ±1.0 TECU; they are not labeled in arbitrary units. The annotated C values range from 0.94 to 1.00 and the A values from 0.23 to 0.46, but neither quantity is defined. They are therefore not interpreted as coherence, confidence, physical amplitude, or a validated directional contrast. Radial, temporal, and azimuthal bin widths, enhancement processing, and the meaning of the dashed diagonals also require source documentation. No propagation speed is obtained from the guide lines.

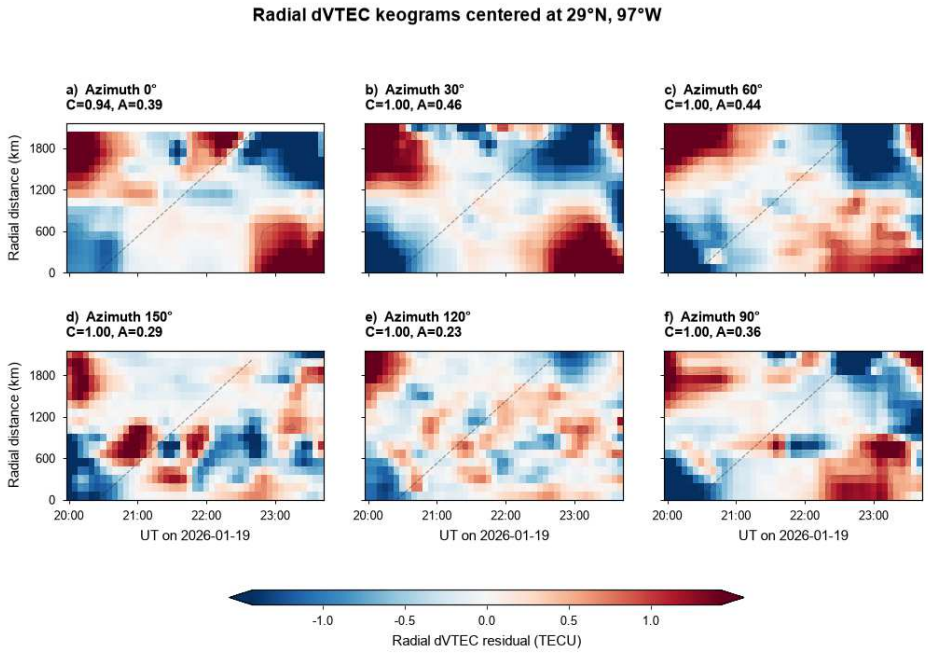


Fig. 7 Radial dVTEC display centered at 29°N, 97°W during 20:00–23:40 UT on 19 January 2026. Panels (a)–(f) carry azimuth labels 0°, 30°, 60°, 150°, 120°, and 90°, respectively, and extend to approximately 2000 km from the reference center. Colors are labeled radial dVTEC residual (TECU), with ticks at −1.0, −0.5, 0, +0.5, and +1.0 and extensions at both ends. The source does not define the C and A annotations, the dashed diagonals, the azimuth convention, bin sizes, or enhancement processing. The reference center is a geometric origin, not an identified disturbance source, and the annotations are retained without a physical or statistical assignment.

3.6 Synthetic Checkerboard Resolution Test

A synthetic checkerboard experiment was supplied to examine the spatial recovery of alternating positive and negative electron-density perturbations under nonuniform observational support (Fig. 8). The prescribed field contains alternating polarity patches with amplitudes spanning -1.0 to $+1.0 \times 10^{11}$ electrons m^{-3}. The experiment is displayed at 225, 325, and 475 km, allowing the recovered horizontal structures and their support patterns to be compared across the three altitude levels.

The recovered fields reproduce the broad alternating-sign organization at all three displayed heights, although the recovered patterns are less spatially complete and less sharply defined than the prescribed checkerboard. Localized departures from the ideal pattern are apparent, particularly near patch boundaries and in areas with weaker or spatially fragmented support. The normalized support maps are strongly heterogeneous: high-support regions form localized clusters rather than a uniform footprint, and their locations and spatial extents vary with altitude. This correspondence indicates that the apparent detail and continuity of the recovered field must be interpreted together with the support diagnostic. In particular, a visually coherent feature in a weak-support

area should not be assigned the same evidential weight as a feature located within a region of stronger observational support.

The supplied figure provides a qualitative, altitude-resolved illustration of checkerboard recovery and spatially varying support. The numerical checkerboard arrays, forward operator, noise realization, inversion settings, and quantitative recovery metrics were not included with the image. We therefore do not infer a numerical resolution length, recovery percentage, error statistic, or altitude-dependent accuracy from the panels alone. The test demonstrates the displayed recovery behaviour under the supplied synthetic setup, but does not by itself establish the resolution or absolute accuracy of the event-derived electron-density fields.

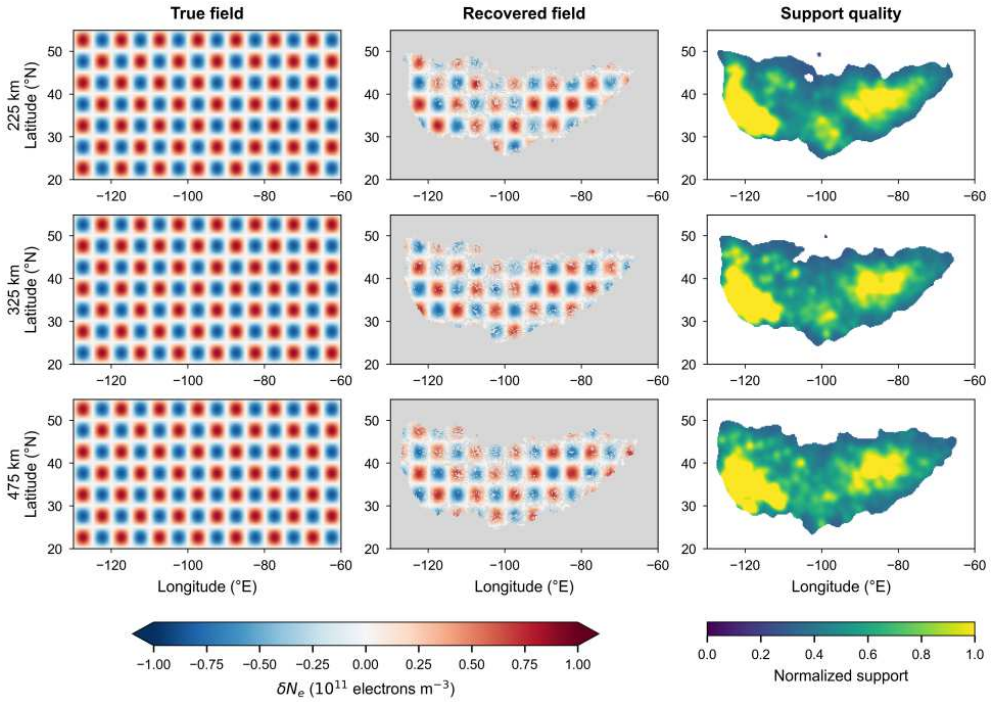


Fig. 8 Synthetic checkerboard resolution test of the three-dimensional ionospheric electron density disturbance reconstruction framework. The three columns show the prescribed true fields, recovered fields, and corresponding normalized support quality, respectively. The three rows represent altitude levels of 225, 325, and 475 km. The synthetic electron density perturbations range from -1.0 to $+1.0 \times 10^{11}$ electrons m^{-3}, with alternating positive and negative spatial patterns. The normalized support quality ranges from 0 to 1, with higher values indicating stronger observational support for the local reconstruction. Gray areas in the recovered-field panels indicate regions outside the displayed reconstruction domain. The experiment evaluates the ability of the reconstruction framework to recover prescribed spatial perturbation structures under nonuniform observational coverage.

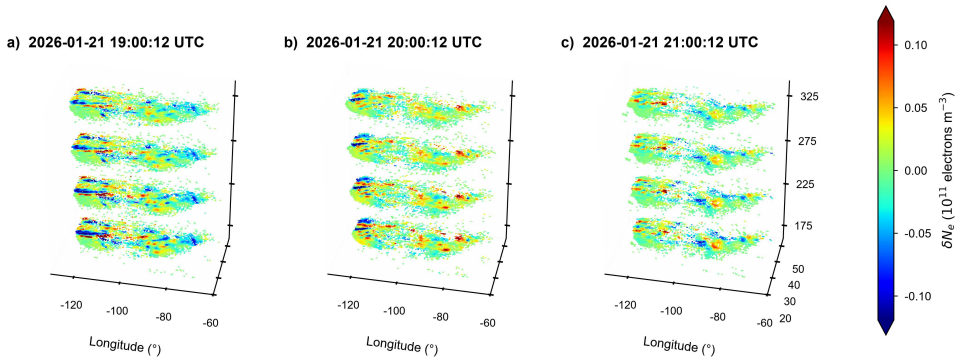


Fig. 9 Altitude-resolved electron-density residuals on 20 January 2026 at (a) 08:00:12, (b) 11:50:12, and (c) 15:30:12 UTC. Horizontal slices are centered at 175, 225, 275, and 325 km and represent the 150–200, 200–250, 250–300, and 300–350 km model layers. Coordinates are geographic longitude, latitude, and height. Colors show signed δN_e in 10^{11} electrons m^{-3}, with common labeled ticks from -0.06 to $+0.06$ in increments of 0.02, equivalent to 2×10^9 electrons m^{-3}. Warm and cool colors indicate positive and negative residuals relative to the adopted background. The 50-km layer spacing is the model discretization, not an independently determined vertical resolution.

3.7 Three-Dimensional Redistribution of the Residual Field

The three-dimensional reconstruction reveals a horizontally structured and altitude-dependent pattern of temporal-residual electron density perturbations over the North American sector on 21 January 2026 (Fig. 9). The snapshots at 19:00:12, 20:00:12, and 21:00:12 UTC provide an hourly sequence spanning 2 h, while the horizontal fields are displayed at 175, 225, 275, and 325 km, giving four altitude levels separated by 50 km across a vertical interval of 150 km. The plotted geographic frame extends approximately from 130°W to 60°W and from 20°N to 50°N, although the reconstructed samples occupy an irregular subset of this domain. At 19:00:12 UTC, alternating positive and negative residuals are evident across the sampled region. In particular, elongated, predominantly zonal bands are visible in the western sector, approximately 125°W–110°W, whereas the central-to-eastern sector, approximately 100°W–75°W, contains more localized and spatially heterogeneous positive and negative features. These broad horizontal patterns recur across the four altitude slices, indicating partial vertical correspondence in the reconstructed disturbance morphology; however, the detailed distribution and continuity of the anomalies differ among altitude levels, demonstrating that the perturbation field is not adequately represented by a vertically uniform structure.

The hourly sequence further shows that the horizontal residual pattern evolves over the 2-h interval. At 20:00:12 UTC, the alternating structures in the western sector remain identifiable, while warm-colored positive residual patches become more conspicuous in parts of the central and eastern sectors, particularly around 90°W–75°W. By 21:00:12 UTC, cool-colored negative residual structures are more prominent across portions of the central sector, approximately 100°W–85°W, while localized positive features remain visible and the western banded pattern is still discernible. The coexistence of positive and negative residuals, together with their differing horizontal organization across the 175–325 km altitude range, points to a spatially heterogeneous storm-time disturbance field rather than a uniform enhancement or depletion of electron density. The color scale is labeled at −0.10, −0.05, 0, +0.05, and +0.10 in units of 10^{11} electrons m^{-3}; these labels establish the displayed perturbation scale but do not, by themselves, provide exact extrema or layer-specific amplitude statistics. Because the figure presents three hourly snapshots rather than a continuously tracked sequence, the apparent displacement or reorganization of individual features cannot be converted into a reliable propagation speed or direction. Likewise, the alternating residual structures alone are insufficient to identify a specific process such as a traveling ionospheric disturbance, storm-enhanced density structure, or equatorial plasma bubble. Such attribution requires complementary time–latitude/longitude keograms, continuous feature tracking, independent observations, and consistency with the event-scale geomagnetic and electrodynamic context. Overall, these horizontal slices demonstrate that the reconstructed temporal-residual field contains organized but altitude-dependent spatial structure over a broad North American region, and they provide a three-dimensional basis for subsequent analyses of disturbance morphology and temporal evolution during the 19–21 January 2026 geomagnetic-storm interval.

The phase-centered maps extend this comparison to the first intensification and later recovery (Fig. 10). The earliest epoch, 18:30:12 on 19 January, precedes the reported sudden storm commencement by approximately 54 min Gordiyenko et al. (2026); it is therefore a pre-commencement comparison, not a sample of the storm's initial compression. Negative residuals of approximately $(4–6) \times 10^9$ electrons m^{-3} in magnitude occur locally around 120°–110°W and 28°–35°N, alongside positive structure in the south-central region. Their presence before commencement also shows why an individual residual feature cannot be attributed to the subsequent storm solely from its sign or geographic location.

Two hours later, at 20:30:12 on 19 January, stronger positive structure appears along parts of the Pacific sector, approximately 125°–115°W and 30°–45°N, and within the south-central region, approximately 110°–100°W and 25°–40°N. Negative residuals remain over portions of the western interior. At 11:50:12 on 20 January, 15 h 20 min after that first-main-phase snapshot, the strongest contrasts include northwest and eastern negative features and central positive residuals of approximately $(4–6) \times 10^9$ electrons m^{-3}. The common 11:50:12 epoch in Figs. 9 and 10 shows corresponding morphology in two representations; this agreement is an internal display consistency, not an independent test of reconstruction accuracy.

At 20:30:12 on 20 January, exactly 24 h after the earlier 20:30:12 snapshot, western positive structure remains around 125°–115°W and 35°–40°N, with negative residuals

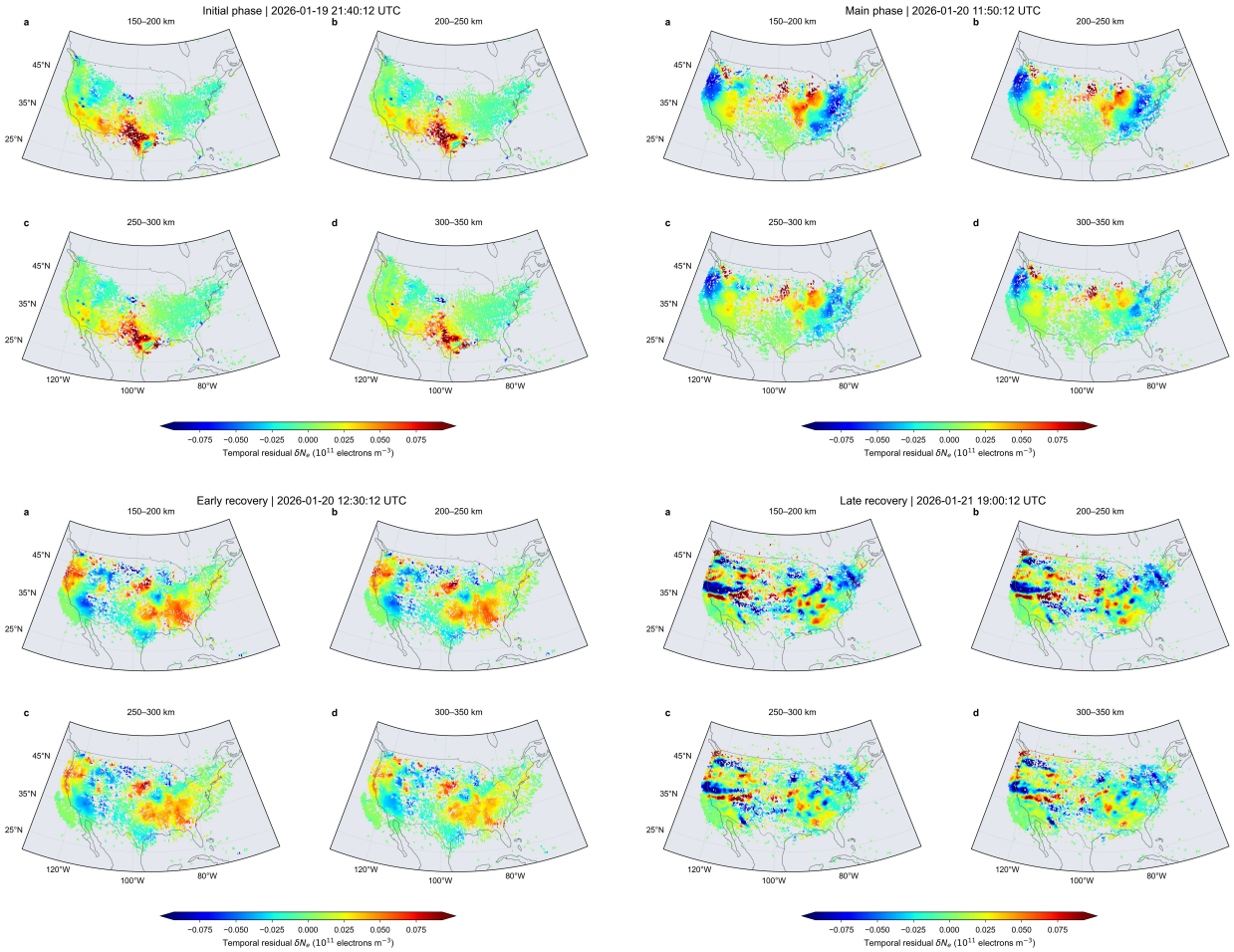


Fig. 10 Electron-density residual maps at four epochs: 19 January 2026 at 18:30:12 and 20:30:12 UTC (upper-left and upper-right groups), and 20 January at 11:50:12 and 20:30:12 UTC (lower-left and lower-right groups). These timestamps represent the pre-commencement interval, first main phase, vicinity of the second SYM-H minimum, and subsequent recovery, respectively; they govern the classification rather than the source image's candidate phase headings. Panels (a)–(d) within each group show the 150–200, 200–250, 250–300, and 300–350 km layers. Coordinates are geographic. Colors give signed temporal δN_e in 10^{11} electrons m^{-3}, using identical labeled ticks from -0.06 to $+0.06$ with increments of 0.02. Gray regions contain no displayed residual values.

of approximately (4–6) $\times 10^9$ electrons m^{-3} locally farther north. Central and eastern contrasts are generally closer to (2–4) $\times 10^9$ electrons m^{-3}. Taken together, the selected fields describe redistribution over a 26-h interval, rather than uniform amplification followed by spatially uniform decay. Their vertical sampling provides additional structure beyond the TEC maps, while the achieved vertical resolution remains an observational question rather than a consequence of the 50-km discretization Muella et al. (2011).

Movies S1, S2, S3, and S5 present the temporal development around the four epochs in Fig. 10, respectively (Supplementary Note S6). Each sequence contains 31 displayed frames over 15 min, with nominal 30-s spacing, across the same four 50-km altitude intervals. This spacing describes the displayed epochs and does not establish a 30-s inversion cadence.

The four selected layers cover 150–350 km, whereas the reconstruction domain contains 18 layers over 100–1000 km. They therefore sample a 200-km portion of the 900-km modeled height range. A feature that is largest at 175 km among these panels is not necessarily the maximum of the complete vertical column. Moreover, the 12-s component of the printed timestamps identifies the displayed epoch; it does not imply a 12-s reconstruction cadence. Both distinctions matter when relating the apparent vertical organization to the fixed spatial and temporal discretization in Section 2.

3.8 Integrated TEC Diagnostics and Altitude-Resolved Residuals

The paired panels compare dVTEC with the reconstructed residual at 325 km, the center of the 300–350 km layer, at the same three epochs on 20 January (Fig. 11). Both diagnostics show negative structure in the south-central sector around 105°–95°W and 27°–33°N at 08:00:12. Local dVTEC values lie near −0.50 to −0.25 TECU, while the selected density layer contains residuals of approximately −(2–4) $\times 10^9$ electrons m^{-3}. In the northeast, around 80°–70°W and 40°–45°N, positive values of approximately +0.25 to +0.50 TECU coincide locally with density residuals of approximately +(2–4) $\times$ 10^9 electrons m^{-3}.

Further local polarity agreement occurs near 11:50:12: negative features are present in both diagnostics around 125°–120°W and 40°–45°N, while positive features overlap around 90°–85°W and 38°–43°N. At 15:30:12, negative structure coincides locally in the northwest, around 125°–120°W and 44°–49°N, and a positive feature occurs in both fields near 98°W, 28°N. Agreement is spatially selective: the 325-km negative core around 105°–95°W and 30°–35°N is accompanied by a geographically mixed dVTEC distribution. It would therefore be inappropriate to assign an opposite or matching sign to the entire south-central region from a single local comparison.

The amplitude scales quantify different observables. A vertically uniform density residual of (4–6) $\times 10^9$ electrons m^{-3} across one 50-km layer would contribute only 0.02–0.03 TECU to a vertical integral, because $\Delta\mathrm{VTEC} = 10^{-16}\delta N_e \Delta h$. This dimensional example is not an estimate of the complete measured column: the remaining heights, their signs, the actual slant paths, and the diagnostic background convention also contribute. Consequently, the plotted density and dVTEC amplitudes cannot be divided to obtain a directly observed layer fraction. The paired maps provide evidence of local co-location and polarity within the available products. Because they derive

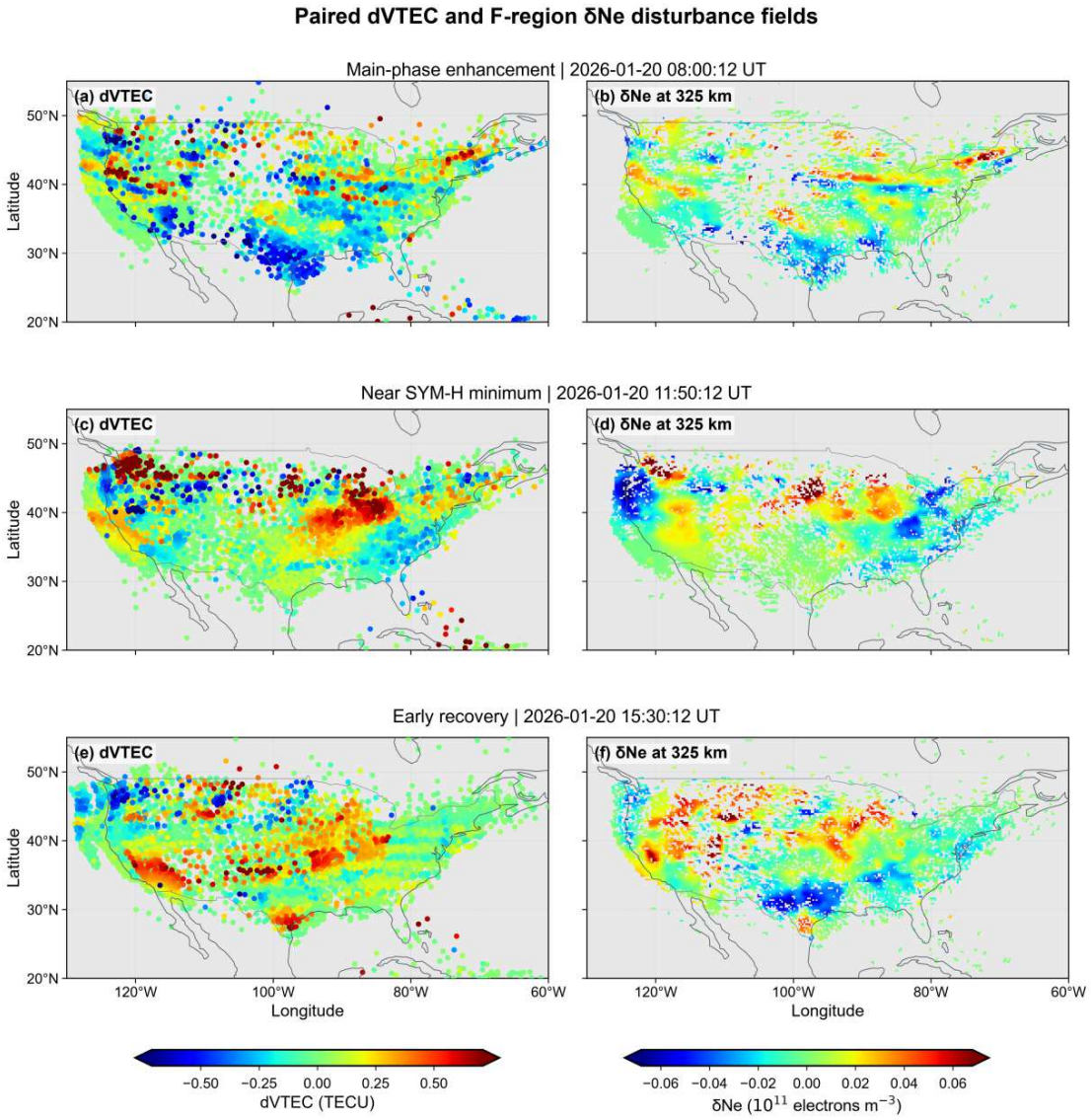


Fig. 11 Paired dVTEC diagnostics and residual electron density at 325 km over North America on 20 January 2026. Rows correspond to 08:00:12, 11:50:12, and 15:30:12 UTC. Panels (a), (c), and (e) show dVTEC (TECU); panels (b), (d), and (f) show δN_e in 10^{11} electrons m^{-3} at the center of the 300–350 km layer. Both columns use geographic coordinates over approximately 130°–60°W and 20°–55°N. Their separate color bars have labeled increments of 0.25 TECU and 0.02×10^{11} electrons m^{-3}, respectively, with extensions at both ends. The first row precedes the second intensification despite its original phase heading. Gray regions contain no displayed values. This comparison concerns regional structure and polarity; the integrated diagnostic and one model layer have different physical supports.

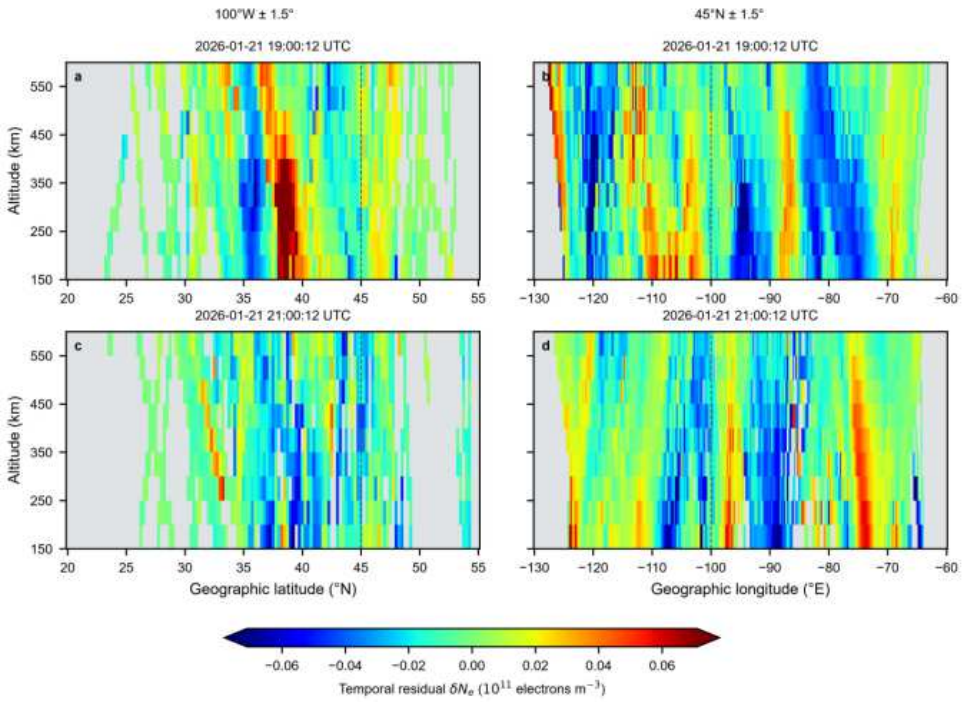


Fig. 12 Orthogonal vertical distributions of the temporal-residual electron density perturbation, δN_e, on 21 January 2026. Panels (a) and (c) show meridional sections centered at 100°W±1.5° at 19:00:12 and 21:00:12 UTC, respectively; panels (b) and (d) show zonal sections centered at 45°N±1.5° at the corresponding epochs. The meridional panels span 20°–55°N, and the zonal panels span 130°–60°W; all panels cover 150–600 km in altitude. Colors represent signed temporal residuals in units of 10^{11} electrons m^{-3}, with positive and negative values indicating enhancements and depletions relative to the adopted temporal background. The labeled color-bar ticks range from −0.06 to +0.06, with extensions at both ends. Dashed lines indicate the central latitude or longitude of each spatial selection; gray regions contain no displayed reconstruction values. Thin black and white contour overlays are retained from the supplied visualization, but their diagnostic definition is not provided and they are not interpreted quantitatively.

from related GNSS observations, they do not establish held-out forward prediction, an independent validation, or a numerical correlation coefficient.

Color contrast is also compared using the numerical legends. The paired dVTEC panels have labeled intervals of 0.25 TECU, whereas the six regional snapshots use 0.2-TECU intervals; the density panels use 2×10^9 electrons m^{-3} intervals. Similar saturation in the two columns consequently does not indicate comparable physical amplitude. This distinction is particularly relevant near 11:50:12, when localized density contrasts coexist with a broad central positive TEC feature, and at 15:30:12, when the selected layer contains a south-central negative core within a mixed integrated field.

3.9 Three-Dimensional Disturbance Morphology and Local Altitude–Time Evolution

Figure 12 presents orthogonal meridional and zonal sections at 19:00:12 and 21:00:12 UTC on 21 January 2026, separated by 120 min. The meridional sections are centered at 100°W within ±1.5° longitude, whereas the zonal sections are centered at 45°N within ±1.5° latitude. All four panels span 150–600 km in altitude. At 19:00:12 UTC, the meridional section shows a pronounced positive residual centered near 38°–39°N and approximately 350–400 km, with local values approaching +0.06 to $+0.07 \times 10^{11}$ electrons m^{-3}. A neighboring negative feature occurs immediately equatorward, near 36°–37°N, and extends through much of the 250–400 km interval, with values approaching −0.06 to -0.07×10^{11} electrons m^{-3}. The juxtaposition of oppositely signed structures over a narrow latitudinal separation demonstrates that the disturbance cannot be represented as a spatially uniform enhancement or depletion. Their different vertical extents also show that the residual field is not vertically uniform.

The corresponding zonal section at 45°N (Fig. 12(b)) exhibits substantial longitudinal heterogeneity across the 130°–60°W interval. Pronounced negative residuals occur near approximately 120°W, 95°W, and 80°W, with local amplitudes approaching -0.06 to -0.07×10^{11} electrons m^{-3}. Positive structures are visible near approximately 110°W and 87°–70°W, with local values reaching about +0.05 to $+0.06 \times 10^{11}$ electrons m^{-3}. The alternating signs extend across multiple altitude levels, indicating that the longitudinal contrasts are not confined to a single horizontal layer. Together, the meridional and zonal sections show that both latitudinal and longitudinal heterogeneity contribute to the reconstructed three-dimensional morphology.

At 21:00:12 UTC, the meridional section (Fig. 12(c)) displays a reorganized residual distribution. A pronounced negative feature is centered near 39°–41°N and approximately 200–300 km, with values approaching -0.06 to -0.07×10^{11} electrons m^{-3}. A localized positive feature occurs farther equatorward, near 32°–34°N and approximately 300–350 km, reaching about +0.04 to $+0.05 \times 10^{11}$ electrons m^{-3}. The zonal section (Fig. 12(d)) likewise contains alternating positive and negative structures, including negative features near approximately 105°W and 90°W and positive features near approximately 97°W and 75°W. The two epochs therefore differ in the locations, signs, and altitude distributions of their strongest residual structures. Because the snapshots do not track uniquely identifiable features continuously, their differences establish temporal reorganization of the total field but do not determine a propagation direction or velocity.

Overall, the orthogonal sections reveal a storm-time residual field with local amplitudes approaching $\pm 0.07 \times 10^{11}$ electrons m^{-3} ($\pm 7 \times 10^{9}$ electrons m^{-3}), substantial horizontal sign contrasts, and altitude-dependent structure. Oppositely signed residuals at neighboring locations and different heights may partly compensate in line-integrated TEC, reinforcing the need to distinguish the three-dimensional distribution from its integral. These observations provide the spatial context for the MP-PET formulation, but the total-field sections alone do not establish the number of independently identifiable components or their individual velocities.

The fixed-location altitude–time section at 80°W, 45°N (Fig. 13) resolves a sequence of positive, negative, and subsequent positive temporal residuals between 19:00 and

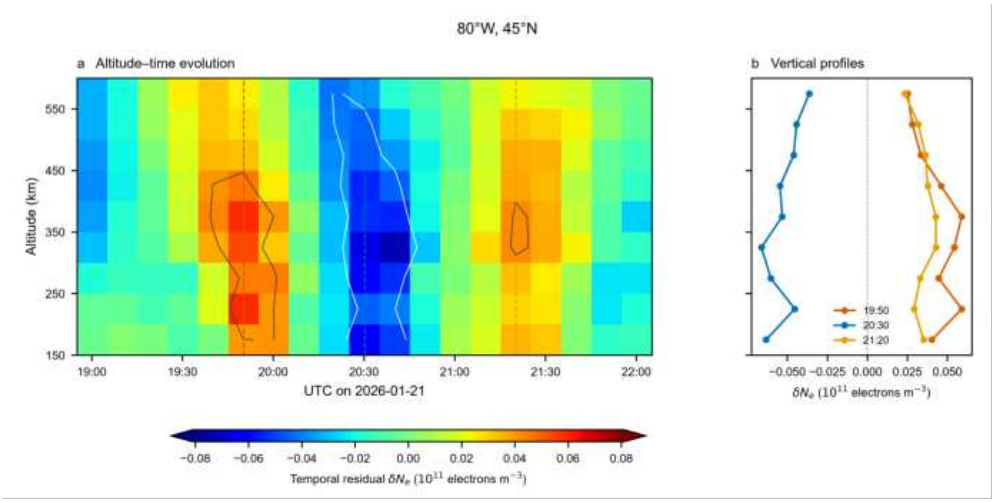


Fig. 13 Altitude–time evolution and vertical profiles of the temporal-residual electron density perturbation, δN_e, at 80°W, 45°N on 21 January 2026. (a) Altitude–time distribution from 19:00 to 22:00 UTC over 150–600 km. (b) Vertical profiles extracted at 19:50, 20:30, and 21:20 UTC, sampled at nine altitude levels from 175 to 575 km with 50-km spacing. The color scale in panel (a) spans -0.08 to $+0.08$ in units of 10^{11} electrons m^{-3}; the profiles are expressed in the same units. Positive and negative values denote enhancements and depletions relative to the adopted temporal background. Dashed vertical lines in panel (a) mark the epochs selected for panel (b). Thin black and white contour overlays are retained from the supplied visualization; their diagnostic definition is not provided and they are not interpreted quantitatively.

22:00 UTC on 21 January. The first positive structure develops mainly between approximately 19:30 and 20:00 UTC and extends from about 200 to 450 km, with its strongest values concentrated near 350–400 km and approaching $+0.06 \times 10^{11}$ electrons m^{-3}. A second positive feature is visible near 200–250 km. The field then changes sign: between approximately 20:15 and 20:50 UTC, a negative structure spans roughly 175–575 km, with the strongest depletion around 275–375 km and amplitudes approaching -0.07×10^{11} electrons m^{-3}. Positive residuals reappear from approximately 21:15 to 21:45 UTC over about 200–550 km, although their peak amplitudes are generally weaker than those of the earlier positive interval. This positive–negative–positive sequence describes the local temporal residual and should not be interpreted, on its own, as a periodic oscillation or as evidence for a single propagating wave.

The three vertical profiles in Fig. 13(b) quantify the altitude dependence of these changes. At 19:50 UTC, the positive residual generally ranges from approximately $+0.025$ to $+0.06 \times 10^{11}$ electrons m^{-3}, with pronounced enhancements near 225 and 375 km. Above approximately 400 km, its magnitude generally decreases toward about $+0.025$ to $+0.035 \times 10^{11}$ electrons m^{-3}. At 20:30 UTC, negative residuals extend across nearly the full sampled altitude interval, 175–575 km. The strongest depletion occurs around 275–325 km and approaches -0.065×10^{11} electrons m^{-3}; the magnitude generally becomes smaller toward the upper levels, although the residual remains negative. Thus, the negative profile is not simply a sign-reversed copy of the earlier

positive profile: its vertical amplitude distribution is distinct, with particularly strong depletion in the lower-middle and middle altitude range.

By 21:20 UTC, the profile is again positive throughout the sampled altitude range, but its magnitude and vertical organization differ from those at 19:50 UTC. The later positive residual is approximately $+0.025$ to $+0.045 \times 10^{11}$ electrons m^{-3}, with its strongest values around 325–375 km. In particular, the enhancement near 225 km is weaker than in the earlier profile, decreasing from approximately $+0.06$ to about $+0.03 \times 10^{11}$ electrons m^{-3}. The return to positive polarity therefore does not represent an exact restoration of the initial vertical structure. Instead, both the amplitude and the relative prominence of individual altitude levels change between the two positive-residual epochs.

Taken together, the fixed-location profiles show that the local residual field changes polarity over the three-hour interval while retaining a distinctly altitude-dependent amplitude distribution. The strongest residuals during the initial positive and intermediate negative intervals are of comparable order, approximately 0.06–0.07×10^{11} electrons m^{-3}, whereas the later positive profile is weaker, reaching approximately 0.045×10^{11} electrons m^{-3}. These observations reinforce the limitation of describing storm-time disturbances at a single altitude or with a spatially uniform temporal constraint. They motivate the MP-PET treatment of horizontal displacement and finite pattern evolution as potentially distinct contributions. However, a fixed-location altitude–time record represents the total residual field and cannot distinguish the passage of an individual structure from local amplitude changes or the superposition of multiple disturbances. Component identifiability and propagation parameters therefore require the subsequent inversion and sensitivity analyses.

4 Discussion

4.1 Information Added by Altitude-Resolved Residuals

The principal event result is the coexistence of regional sign contrasts and systematic altitude dependence during geomagnetic recovery. In Fig. 4, the change in SYM-H from -244 to -90 nT represents a 63% reduction in magnitude; the 21 January 20:00 snapshot still contains localized positive and negative TEC residuals near the 0.6–0.8 TECU color levels. The orthogonal sections in Fig. 12 show local density residuals approaching $\pm 0.07 \times 10^{11}$ electrons m^{-3} at 19:00:12 and 21:00:12 UTC, with alternating signs across latitude and longitude. At 80°W, 45°N, Fig. 13 further shows a positive–negative–positive sequence over three hours, with the strongest selected profiles reaching approximately $+0.06$, -0.065, and $+0.045 \times 10^{11}$ electrons m^{-3}. The vertical distributions differ among these epochs, demonstrating that neither a single storm index nor an integrated TEC value specifies the local altitude organization of the residual field. The contribution of the altitude-resolved description is to locate the residual structure and quantify its amplitude distribution, rather than to infer an absolute density enhancement from a detrended field.

This interpretation is consistent with established tomography limitations and with the concurrent disturbances reported over the American sector during this storm Yeh and Raymund (1991); Guan et al. (2026); Muella et al. (2011). It does not require that

every patch belong to one freely propagating gravity wave. Storm-enhanced density gradients, evolving electrodynamic conditions, and neutral-wave disturbances can overlap Buonsanto (1999); Zhang et al. (2022). The present figures do not separate these drivers. In particular, the positive–negative–positive sequence at a fixed location documents temporal sign reversal, not a demonstrated periodic oscillation or a uniquely tracked wave. Nor does a height-dependent amplitude profile establish upward energy propagation: phase information, a compatible background, and independent vertical constraints would be needed.

4.2 Methodological Contribution and Its Limits

MP-PET addresses a specific limitation of temporal regularization by allowing coherent horizontal displacement and local pattern evolution to coexist. Its component-number correction removes the reduction in quadratic cost produced by identical duplication, while profiling reoptimizes density and increments at each tested propagation field. These properties complement established time-dependent tomography and joint motion-reconstruction approaches Mitchell and Spencer (2003); Spencer and Mitchell (2007); Burger et al. (2018); Gris et al. (2020). They do not prove that two components improve reconstruction, that the joint problem has a unique physical solution, or that a selected pattern velocity measures plasma transport. The conditional sensitivity construction makes this distinction explicit: information about propagation cannot increase when additional competing increment directions are admitted, and unrestricted increments can remove that information entirely.

The twelve main-text event figures support interpretation of the displayed total field. The additional supplementary diagnostics report their stated predictive and held-out comparisons, but they are not accompanied by an archived end-to-end MP-PET run or independent validation of the altitude allocation. Component-resolved validation from an archived MP-PET run is likewise absent. Consequently, an accuracy gain, a preferred component count, and a speed distribution cannot be claimed here. The proposed contribution is the explicit formulation and its mathematical qualifications, accompanied by a quantitative event description. Demonstrating an empirical advantage requires executing the stated protocol with the actual geometry, retaining failed and unresolved cases, and linking every result to its processing configuration. Agreement between TEC maps and density maps derived from related GNSS observations is a consistency check, not independent validation.

4.3 Background, Resolution, and Reproducibility

The inferred state is an observation-compatible residual under a specified background convention. A centered 60 min filter has gains of approximately 0.873 and 1.161 at 25 and 50 min, respectively; its amplitude response alone can change comparisons between spectral components. These analytical gains cannot correct an unknown figure-processing history. Moreover, filtering moving ray integrals is not generally equivalent to integrating a pointwise filtered density field. Preprocessing controls must therefore accompany tests of the inversion itself Guerra et al. (2024).

Vertical interpretation is also limited by measurement geometry. A 50 km layer thickness and a complete 18-mode basis do not demonstrate 50 km resolution or prior-independent structure Bust and Mitchell (2008); Mei et al. (2023b); Muella et al. (2011). The new sections show altitude-dependent residual morphology, but the displayed grid spacing and spatial selection widths are not measurements of achieved vertical or horizontal resolution. The thin contour overlays in Figs. 12 and 13 also lack a documented diagnostic definition and are therefore excluded from quantitative interpretation. Compatible independent profiles, resolution tests, and complete figure provenance are necessary before the displayed altitude structure can be treated as a validated reconstruction of the storm.

5 Conclusions

The North American figures for 19–22 January 2026 show substantial residual structure during geomagnetic recovery. SYM-H changed from -244 to -90 nT between the selected 20 and 21 January maps, a reduction of approximately 63% in absolute magnitude, while the 21 January 20:00 snapshot retained localized TEC residuals near ± 0.6–0.8 TECU. The orthogonal density sections at 100°W and 45°N on 21 January show alternating positive and negative structures with local amplitudes approaching $\pm 0.07 \times 10^{11}$ electrons m^{-3}. At 80°W, 45°N, the altitude–time section exhibits a positive–negative–positive residual sequence between 19:00 and 22:00 UTC, with selected vertical-profile extrema of approximately $+0.06$, -0.065, and $+0.045 \times 10^{11}$ electrons m^{-3}. The differing vertical profiles show that the return to positive polarity does not imply restoration of the earlier altitude structure. These displayed fields quantify aspects of the disturbance distribution that an integrated TEC map does not uniquely specify.

MP-PET provides an explicit framework for separating horizontal pattern displacement from finite residual evolution. Its mathematical contribution comprises duplication-corrected regularization, profiled propagation estimation, and conditional identifiability diagnostics. These results justify treating the total field as primary and withholding unsupported component interpretations.

The present evidence establishes a quantitative description of the supplied event figures and a qualified inversion framework. It does not establish an event-specific accuracy gain, a resolved two-pattern decomposition, or a unique disturbance mechanism. Archived inversion runs, preprocessing-consistent independent profiles, and the specified synthetic and withheld-data comparisons are required to test those stronger claims.

Data and Code Availability

The multi-GNSS data used in this study are available from the GEONET network. Precise orbit (SP3) products were obtained from Wuhan University (WHU) and the European Space Agency (ESA). We have made the GNSS-TEC algorithm presented in this paper available to readers for experience and learning purposes. It can be accessed at http://8.130.36.30/tec/tec2d.

Acknowledgements

Funding

This research was funded by the National Key R&D Program of China (Grant No. 2025YFE0115800); the Guangxi Science and Technology Project (Grant Nos. 2026GXNSFAA00640119, GuikeAB25069126, GuikeAA24206043, GuikeAA24263010, GuikeAA24263029, and GuikeAA24206025); the National Natural Science Foundation of China (Grant Nos. U25A20397, U23A20280, 62661019, and 62471153); the Guangxi Major Talent Project; the Guangxi University Young and Middle-aged Teachers Basic Scientific Research Ability Improvement Project (Grant No. 2025KY0831); the Key Laboratory of Cognitive Radio and Information Processing, Ministry of Education, China (Grant No. CRKL230104); and the Innovation Project of Guangxi Graduate Education (Grant No. YCBZ2024171).

Declarations

Competing interests

The authors declare that they have no competing interests.

References

Austen, J.R., Franke, S.J., Liu, C.H.: Ionospheric imaging using computerized tomography. Radio Sci. **23**(3), 299–307 (1988) https://doi.org/10.1029/RS023i003p00299

Aa, E., Forsythe, V.V., Zhang, S.-R., Wang, W., Coster, A.J.: Next-decade needs for 3-D ionosphere imaging. Front. Astron. Space Sci. **10** (2023) https://doi.org/10.3389/fspas.2023.1186513 . Art. no. 1186513

Angling, M.J.: First assimilations of COSMIC radio occultation data into the Electron Density Assimilative Model (EDAM). Ann. Geophys. **26**(2), 353–359 (2008) https://doi.org/10.5194/angeo-26-353-2008

Burger, M., Dirks, H., Schönlieb, C.-B.: A variational model for joint motion estimation and image reconstruction. SIAM J. Imaging Sci. **11**(1), 94–128 (2018) https://doi.org/10.1137/16M1084183

Bust, G.S., Garner, T.W., Gaussiran, T.L. II: Ionospheric Data Assimilation Three-Dimensional (IDA3D): A global, multisensor, electron density specification algorithm. J. Geophys. Res. **109**(A11) (2004) https://doi.org/10.1029/2003JA010234 . Art. no. A11312

Bust, G.S., Mitchell, C.N.: History, current state, and future directions of ionospheric imaging. Rev. Geophys. **46**(1) (2008) https://doi.org/10.1029/2006RG000212 . Art. no. RG1003

Bilitza, D., Pezzopane, M., Truhlik, V., Altadill, D., Reinisch, B.W., Pignalberi, A.: The International Reference Ionosphere model: A review and description of an ionospheric benchmark. Rev. Geophys. **60**(4) (2022) https://doi.org/10.1029/2022RG000792 . Art. no. e2022RG000792

Buonsanto, M.J.: Ionospheric storms—A review. Space Sci. Rev. **88**(3-4), 563–601 (1999) https://doi.org/10.1023/A:1005107532631

Chambolle, A., Pock, T.: A first-order primal-dual algorithm for convex problems with applications to imaging. J. Math. Imaging Vis. **40**(1), 120–145 (2011) https://doi.org/10.1007/s10851-010-0251-1

Candès, E.J., Romberg, J., Tao, T.: Robust uncertainty principles: Exact signal reconstruction from highly incomplete frequency information. IEEE Trans. Inf. Theory **52**(2), 489–509 (2006) https://doi.org/10.1109/TIT.2005.862083

Coster, A., Williams, J., Weatherwax, A., Rideout, W., Herne, D.: Accuracy of GPS total electron content: GPS receiver bias temperature dependence. Radio Sci. **48**(2), 190–196 (2013) https://doi.org/10.1002/rds.20011

Donoho, D.L.: Compressed sensing. IEEE Trans. Inf. Theory **52**(4), 1289–1306 (2006) https://doi.org/10.1109/TIT.2006.871582

Ding, F., Wan, W., Ning, B., Wang, M.: Large-scale traveling ionospheric disturbances observed by GPS total electron content during the magnetic storm of 29–30 October 2003. J. Geophys. Res. **112**(A6) (2007) https://doi.org/10.1029/2006JA012013 . Art. no. A06309

Emmert, J.T., Richmond, A.D., Drob, D.P.: A computationally compact representation of Magnetic-Apex and Quasi-Dipole coordinates with smooth base vectors. J. Geophys. Res. Space Phys. **115**(A8) (2010) https://doi.org/10.1029/2010JA015326 . Art. no. A08322

Fritts, D.C., Vadas, S.L.: Gravity wave penetration into the thermosphere: Sensitivity to solar cycle variations and mean winds. Ann. Geophys. **26**(12), 3841–3861 (2008) https://doi.org/10.5194/angeo-26-3841-2008

Gris, B., Chen, C., Öktem, O.: Image reconstruction through metamorphosis. Inverse Problems **36**(2) (2020) https://doi.org/10.1088/1361-6420/ab5832 . Art. no. 025001

Guerra, M., Cesaroni, C., Ravanelli, M., Spogli, L.: Travelling ionospheric disturbances detection: A statistical study of detrending techniques, induced period error and near real-time observables. J. Space Weather Space Clim. **14** (2024) https://doi.org/10.1051/swsc/2024017 . Art. no. 17

Gordiyenko, G., Litvinov, Y., Zhiganbayev, M., Grichshenko, V., Nurakynov, S., Andreyev, A., Zhigalov, V.: Ionospheric response to the severe geomagnetic storm of

19–21 January 2026 over Almaty (Kazakhstan) according to the Digisonde and GPS data. Sensors **26**(18) (2026) https://doi.org/10.3390/s26185935 . Art. no. 5935

Golub, G.H., Pereyra, V.: The differentiation of pseudo-inverses and nonlinear least squares problems whose variables separate. SIAM J. Numer. Anal. **10**(2), 413–432 (1973) https://doi.org/10.1137/0710036

Guan, X., Xu, W., Li, W., Meng, X., Pan, X., Zhao, D., Zhang, K.: Spatiotemporal features of concurrent storm-time ionospheric disturbances over the American sector during the January 2026 geomagnetic storm. J. Geophys. Res. Space Phys. **131**(7) (2026) https://doi.org/10.1029/2026JA035553 . Art. no. e2026JA035553

Hines, C.O.: Internal atmospheric gravity waves at ionospheric heights. Can. J. Phys. **38**(11), 1441–1481 (1960) https://doi.org/10.1139/p60-150

Hernández-Pajares, M., Juan, J.M., Sanz, J.: Medium-scale traveling ionospheric disturbances affecting GPS measurements: Spatial and temporal analysis. J. Geophys. Res. **111**(A7) (2006) https://doi.org/10.1029/2005JA011474 . Art. no. A07S11

Howe, B.M., Runciman, K., Secan, J.A.: Tomography of the ionosphere: Four-dimensional simulations. Radio Sci. **33**(1), 109–128 (1998) https://doi.org/10.1029/97RS02615

Hocke, K., Schlegel, K.: A review of atmospheric gravity waves and travelling ionospheric disturbances: 1982–1995. Ann. Geophys. **14**(9), 917–940 (1996) https://doi.org/10.1007/s00585-996-0917-6

Huber, P.J.: Robust estimation of a location parameter. Ann. Math. Stat. **35**(1), 73–101 (1964) https://doi.org/10.1214/aoms/1177703732

Hunsucker, R.D.: Atmospheric gravity waves generated in the high-latitude ionosphere: A review. Rev. Geophys. **20**(2), 293–315 (1982) https://doi.org/10.1029/RG020i002p00293

Karan, D.K., Eastes, R.W., Pandey, K., Wang, W., Martinis, C.R., Daniell, R.E., Gan, Q.: Post-sunset merging of equatorial ionization anomaly crests into a single peak over $\sim 35^\circ$ longitude during the 19 January 2026 geomagnetic superstorm. Geophys. Res. Lett. **53**(16) (2026) https://doi.org/10.1029/2026GL124019 . Art. no. e2026GL124019

Keys, R.G.: Cubic convolution interpolation for digital image processing. IEEE Trans. Acoust., Speech, Signal Process. **29**(6), 1153–1160 (1981) https://doi.org/10.1109/TASSP.1981.1163711

Kong, J., Li, F., Yao, Y., Wang, Z., Peng, W., Zhang, Q.: Reconstruction of 2D/3D ionospheric disturbances in high-latitude and arctic regions during a geomagnetic storm using GNSS carrier TEC: A case study of the 2015 great storm. J. Geod.

93(9), 1529–1541 (2019) https://doi.org/10.1007/s00190-019-01266-6

Krah, P., Marmin, A., Zorawski, B., Reiss, J., Schneider, K.: A robust shifted proper orthogonal decomposition: Proximal methods for decomposing flows with multiple transports. SIAM J. Sci. Comput. **47**(2), 633–656 (2025) https://doi.org/10.1137/24M164392X

Künsch, H.R.: The jackknife and the bootstrap for general stationary observations. Ann. Stat. **17**(3), 1217–1241 (1989) https://doi.org/10.1214/aos/1176347265

Li, C., Fang, H., Xiao, C., Duan, D., Lin, Y., Huang, H., Ren, G., Wu, H., Zhou, C., Zheng, H., Shen, X., Cao, X.: TEC2Ne: A physics-informed deep learning framework for reconstructing ionospheric electron density profiles from global TEC maps. GPS Solut. **30**(4) (2026) https://doi.org/10.1007/s10291-026-02112-x . Art. no. 172

Liang, W., Sun, X., Ji, Y., Ren, X., Jia, X., Chen, Q.: Three-dimensional reconstruction of ionospheric disturbance structures during the pre-storm phase of the 10–11 May 2024 geomagnetic storm using a compressed sensing-based tomographic technique. Adv. Space Res. **77**(9), 9662–9674 (2026) https://doi.org/10.1016/j.asr.2026.02.041

Liang, W., Sun, X., Ji, Y., Ren, X.: Ionospheric response to the 8 April 2024 total solar eclipse: Plasma depletion and eclipse-driven MsTIDs. Space Weather **24**(4) (2026) https://doi.org/10.1029/2025SW004703 . Art. no. e2025SW004703

Mallat, S.G.: A theory for multiresolution signal decomposition: The wavelet representation. IEEE Trans. Pattern Anal. Mach. Intell. **11**(7), 674–693 (1989) https://doi.org/10.1109/34.192463

Muella, M.T.A.H., Paula, E.R., Mitchell, C.N., Kintner, P.M., Paes, R.R., Batista, I.S.: Tomographic imaging of the equatorial and low-latitude ionosphere over central-eastern Brazil. Earth Planets Space **63**(2), 129–138 (2011) https://doi.org/10.5047/eps.2010.12.011

Ma, J., Fu, H., Huba, J.D., Jin, Y.: A novel ionospheric inversion model: PINN-SAMI3 (physics informed neural network based on SAMI3). Space Weather **22**(4) (2024) https://doi.org/10.1029/2023SW003823 . Art. no. e2023SW003823

Makela, J.J., Otsuka, Y.: Overview of nighttime ionospheric instabilities at low- and mid-latitudes: Coupling aspects resulting in structuring at the mesoscale. Space Sci. Rev. **168**(1-4), 419–440 (2012) https://doi.org/10.1007/s11214-011-9816-6

Mei, D., Ren, X., Le, X., Liu, H., Zhang, X.: Ionospheric tomography: A compressed sensing technique based on dictionary learning. IEEE Trans. Geosci. Remote Sens. **61**, 1–10 (2023) https://doi.org/10.1109/TGRS.2023.3252041

Mei, D., Ren, X., Liu, H., Le, X., Xiong, S., Zhang, X.: Global three-dimensional ionospheric tomography by combination of ground-based and space-borne GNSS

data. Space Weather **21**(4) (2023) https://doi.org/10.1029/2022SW003368 . Art. no. e2022SW003368

Mitchell, C.N., Spencer, P.S.J.: A three-dimensional time-dependent algorithm for ionospheric imaging using GPS. Ann. Geophys. **46**(4), 687–696 (2003) https://doi.org/10.4401/ag-4373

Mannucci, A.J., Wilson, B.D., Yuan, D.N., Ho, C.H., Lindqwister, U.J., Runge, T.F.: A global mapping technique for GPS-derived ionospheric total electron content measurements. Radio Sci. **33**(3), 565–582 (1998) https://doi.org/10.1029/97RS02707

Penney, R.W., Jackson-Booth, N.K.: Mitigating satellite motion in GPS monitoring of traveling ionospheric disturbances. Radio Sci. **50**(11), 1150–1164 (2015) https://doi.org/10.1002/2015RS005767

Panicciari, T., Smith, N.D., Mitchell, C.N., Da Dalt, F., Spencer, P.S.J.: Using sparse regularization for multi-resolution tomography of the ionosphere. Nonlin. Processes Geophys. **22**(5), 613–624 (2015) https://doi.org/10.5194/npg-22-613-2015

Raymund, T.D., Austen, J.R., Franke, S.J., Liu, C.H., Klobuchar, J.A., Stalker, J.: Application of computerized tomography to the investigation of ionospheric structures. Radio Sci. **25**(5), 771–789 (1990) https://doi.org/10.1029/RS025i005p00771

Roberts, D.R., Bahn, V., Ciuti, S., Boyce, M.S., Elith, J., Guillera-Arroita, G., Hauenstein, S., Lahoz-Monfort, J.J., Schröder, B., Thuiller, W., Warton, D.I., Wintle, B.A., Hartig, F., Dormann, C.F.: Cross-validation strategies for data with temporal, spatial, hierarchical, or phylogenetic structure. Ecography **40**(8), 913–929 (2017) https://doi.org/10.1111/ecog.02881

Rideout, W., Coster, A.: Automated GPS processing for global total electron content data. GPS Solut. **10**(3), 219–228 (2006) https://doi.org/10.1007/s10291-006-0029-5

Raue, A., Kreutz, C., Maiwald, T., Bachmann, J., Schilling, M., Klingmüller, U., Timmer, J.: Structural and practical identifiability analysis of partially observed dynamical models by exploiting the profile likelihood. Bioinformatics **25**(15), 1923–1929 (2009) https://doi.org/10.1093/bioinformatics/btp358

Ren, X., Mei, D., Liu, H., Zhang, X.: Investigation on horizontal and vertical traveling ionospheric disturbances propagation in global-scale using GNSS and multi-LEO satellites. Space Weather **20**(5) (2022) https://doi.org/10.1029/2022SW003041 . Art. no. e2022SW003041

Reiss, J., Schulze, P., Sesterhenn, J., Mehrmann, V.: The shifted proper orthogonal decomposition: A mode decomposition for multiple transport phenomena. SIAM J. Sci. Comput. **40**(3), 1322–1344 (2018) https://doi.org/10.1137/17M1140571

Saito, A., Fukao, S., Miyazaki, S.: High resolution mapping of TEC perturbations with

the GSI GPS Network over Japan. Geophys. Res. Lett. **25**(16), 3079–3082 (1998) https://doi.org/10.1029/98GL52361

Spencer, P.S.J., Mitchell, C.N.: Imaging of fast moving electron-density structures in the polar cap. Ann. Geophys. **50**(3), 427–434 (2007) https://doi.org/10.4401/ag-3074

Schunk, R.W., Scherliess, L., Sojka, J.J., Thompson, D.C., Anderson, D.N., Codrescu, M., Minter, C., Fuller-Rowell, T.J., Heelis, R.A., Hairston, M., Howe, B.M.: Global Assimilation of Ionospheric Measurements (GAIM). Radio Sci. **39**(1) (2004) https://doi.org/10.1029/2002RS002794 . Art. no. RS1S02

Scherliess, L., Schunk, R.W., Sojka, J.J., Thompson, D.C., Zhu, L.: Utah State University Global Assimilation of Ionospheric Measurements Gauss-Markov Kalman filter model of the ionosphere: Model description and validation. J. Geophys. Res. **111**(A11) (2006) https://doi.org/10.1029/2006JA011712 . Art. no. A11315

Leeuwen, T., Aravkin, A.Y.: Variable projection for nonsmooth problems. SIAM J. Sci. Comput. **43**(5), 249–268 (2021) https://doi.org/10.1137/20M1348650

Vadas, S.L., Nicolls, M.J.: The phases and amplitudes of gravity waves propagating and dissipating in the thermosphere: Theory. J. Geophys. Res. **117**(A5) (2012) https://doi.org/10.1029/2011JA017426 . Art. no. A05322

Yeh, K.C., Raymund, T.D.: Limitations of ionospheric imaging by tomography. Radio Sci. **26**(6), 1361–1380 (1991) https://doi.org/10.1029/91RS01873

Zhang, S.-R., Nishimura, Y., Erickson, P.J., Aa, E., Kil, H., Deng, Y., Thomas, E.G., Rideout, W., Coster, A.J., Kerr, R., Vierinen, J.: Traveling ionospheric disturbances in the vicinity of storm-enhanced density at midlatitudes. J. Geophys. Res. Space Phys. **127**(8) (2022) https://doi.org/10.1029/2022JA030429 . Art. no. e2022JA030429

Zhao, J., Tang, Q., Zhou, C., Zhao, Z., Wei, F.: Three-dimensional ionospheric tomography based on compressed sensing. GPS Solut. **27**(2) (2023) https://doi.org/10.1007/s10291-023-01427-3 . Art. no. 90

Supplementary Files

This is a list of supplementary files associated with this preprint. Click to download.

- supplement.pdf
- movies.rar